UCSF

UC San Francisco Previously Published Works

Title

Structure of a Prokaryotic Sodium Channel Pore Reveals Essential Gating Elements and an Outer Ion Binding Site Common to Eukaryotic Channels

Permalink

https://escholarship.org/uc/item/71h0m6d9

Journal

Journal of Molecular Biology, 426(2)

ISSN

0022-2836

Authors

Shaya, David
Findeisen, Felix
Abderemane-Ali, Fayal
et al.

Publication Date

2014

DOI

10.1016/j.jmb.2013.10.010

Peer reviewed

eScholarship.org Powered by the California Digital Library
University of California

# Structure of a Prokaryotic Sodium Channel Pore Reveals Essential Gating Elements and an Outer Ion Binding Site Common to Eukaryotic Channels

**David Shaya[1,†], Felix Findeisen[1,†], Fayal Abderemane-Ali[2,3,4], Cristina Arrigoni[1], Stephanie Wong[1], Shailika Reddy Nurva[1], Gildas Loussouarn[2,3,4] and Daniel L. Minor Jr.[1,5,6,7]**

*1 - **Cardiovascular Research Institute,** University of California, San Francisco, CA 94158-9001, USA*
*2 - **Institut National de la Santé et de la Recherche Médicale,** UMR 1087, F-44000 Nantes, France*
*3 - **Centre National de la Recherche Scientifique,** UMR 6291, F-44000 Nantes, France*
*4 - **L'institut du thorax,** L'UNAM, Université de Nantes, F-44000 Nantes, France*
*5 - **Departments of Biochemistry and Biophysics and Cellular and Molecular Pharmacology,** University of California, San Francisco, CA 94158-9001, USA*
*6 - **California Institute for Quantitative Biomedical Research,** University of California, San Francisco, CA 94158-9001, USA*
*7 - **Physical Biosciences Science Division,** Lawrence Berkeley National Laboratory, Berkeley, CA 94720, USA*

***Correspondence to Daniel L. Minor:** Cardiovascular Research Institute, University of California, San Francisco, CA 94158-9001, USA. daniel.minor@ucsf.edu*
http://dx.doi.org/10.1016/j.jmb.2013.10.010
***Edited by Y. Shi***

## Abstract

Voltage-gated sodium channels ($Na_V$s) are central elements of cellular excitation. Notwithstanding advances from recent bacterial $Na_V$ ($BacNa_V$) structures, key questions about gating and ion selectivity remain. Here, we present a closed conformation of $Na_V$Ae1p, a pore-only $BacNa_V$ derived from $Na_V$Ae1, a $BacNa_V$ from the arsenite oxidizer *Alkalilimnicola ehrlichei* found in Mono Lake, California, that provides insight into both fundamental properties. The structure reveals a pore domain in which the pore-lining S6 helix connects to a helical cytoplasmic tail. Electrophysiological studies of full-length $BacNa_V$s show that two elements defined by the $Na_V$Ae1p structure, an S6 activation gate position and the cytoplasmic tail "neck", are central to $BacNa_V$ gating. The structure also reveals the selectivity filter ion entry site, termed the "outer ion" site. Comparison with mammalian voltage-gated calcium channel ($Ca_V$) selectivity filters, together with functional studies, shows that this site forms a previously unknown determinant of $Ca_V$ high-affinity calcium binding. Our findings underscore commonalities between $BacNa_V$s and eukaryotic voltage-gated channels and provide a framework for understanding gating and ion permeation in this superfamily.

© 2013 The Authors. Published by Elsevier Ltd. All rights reserved.

## Introduction

Voltage-gated sodium channels ($Na_V$s) are large, multipass membrane proteins that are critical for cellular excitation [1,2]. These channels are targets for drugs directed at neuropathic pain, migraine, arrhythmias, and epilepsy [3,4], as well as environmental toxins [5]. $Na_V$s belong to the voltage-gated ion channel (VGIC) superfamily and are most closely related to voltage-gated calcium channels ($Ca_V$s) [6,7]. Despite ion selectivity differences, mutational studies [8–10] and sequence similarities [6,7] have suggested that $Na_V$s and $Ca_V$s share similar selectivity filter architectures [2]. However, details of this presumed commonality are unknown.

Discovery of a large family of bacterial $Na_V$s ($BacNa_V$s) [11–13] that may be ancestors of eukaryotic $Na_V$s and $Ca_V$s [14] has enabled delineation of structural principles shared by this VGIC superfamily branch. $BacNa_V$s are tetramers. Each subunit has six transmembrane segments that comprise a voltage-sensing domain (VSD) composed of the S1–S4 segments and a pore domain (PD) formed from the S5–S6 segments [15–17]. This subunit architecture is

recapitulated in eukaryotic $Na_V$s and $Ca_V$s where four homologous six-transmembrane repeats occur in a single polypeptide [2,6,7]. Protein dissection studies have demonstrated a further modular aspect of $BacNa_V$ architecture within the membrane domains. $BacNa_V$ "pore-only" constructs lacking the VSD have been demonstrated to fold [18–20], assemble [18–20], and form functional, selective ion channels [19]. These demonstrations of $BacNa_V$ modularity are in accord with various lines of evidence that support the independence of the VSDs and PDs. These include: the fact that within the VGIC family, potassium channels occur two forms, those that encompass a PD alone (Kir and $K_{2P}$ channels) and those having a VSD attached to the PD [6,7], results from VSD-PD chimera studies [21–24] and structural evidence indicating that VSDs and PDs lack extensive contacts [15–17,25–27]. Although recent $BacNa_V$ structures have revealed the basic transmembrane architecture [15–17,20], fundamental questions about gating, ion permeation, and ion selectivity have remained unanswered.

$BacNa_V$s have a conserved ~40-residue C-terminal cytoplasmic tail [28,29] that is important for assembly [28] and function [29,30]. However, this domain is either unresolved [15,16] or absent from the crystallized constructs [17,20] of prior $BacNa_V$ structures. Hence, its structure, relationship to the PD, and key functional elements have remained enigmatic.

Ion permeation is fundamental ion channel property [2]. Original descriptions of the $BacNa_V$ $Na_VAb$ suggested a single ion pore model [15]. In contrast, functional studies of $Na_V$s [2,31] and $Ca_V$s [2,32] support the presence of multi-ion pores as a means to affect ion selectivity and permeation [33,34]. To date, only a single $BacNa_V$ ion binding site has been observed at the inner vestibule of the $Na_VRh$ selectivity filter [17]. Recent computational studies have suggested the possibility of other ion binding sites [35,36], but the absence of experimental data have left unresolved questions regarding the existence of such sites, their exact locations, and residues involved in ion binding.

Here, we present the structure of $Na_VAe1p$, a pore-only sodium channel derived from the *Alkalilimnicola ehrlichei* $BacNa_V$ $Na_VAe1$ [19]. The structure shows a closed conformation of a complete PD and cytoplasmic tail. Functional tests of key structural elements suggest that $BacNa_V$ opening involves changes at an S6 activation gate residue and a structural rearrangement in the neck region of the cytoplasmic tail. The structure also reveals an ion binding site in the selectivity filter that we term the "outer ion" site. We demonstrate that the ion coordination residue comprising this site has a previously unrecognized counterpart in mammalian $Ca_V$s that is crucial to high-affinity calcium binding, a result that lends support to long-standing proposals regarding the presence of multiple ion binding sites in $Ca_V$s [32–34]. Together, our results emphasize the deep evolutionary links between $BacNa_V$s and mammalian channels and suggest that channels sharing this selectivity filter architecture have multiple ion binding sites.

## Results

### Structure of the pore-only channel $Na_VAe1p$

We determined the structure of $Na_VAe1p$, a "pore-only" protein bearing the PD and cytoplasmic tail of the $BacNa_V$ $Na_VAe1$ [19] (Table S1) using X-ray diffraction data obtained from a *I*222 crystal that diffracted to a resolution of 4.00 Å based on traditional measures such as $R_{pim}$ or $I\sigma/I$. However, as it has been shown recently that adding weak high-resolution data beyond the commonly arbitrarily defined cutoffs used to judge resolution limits may be beneficial [37–39], we used data to a resolution of 3.46 Å based on CC (*c*orrelation *c*oefficient) evaluation ($CC_{1/2} > 0.1$) [37]. Molecular replacement using a PD ensemble from the *Arcobacter butzleri* ($Na_VAb$) [15,16] and *Rickettsia* sp. ($Na_VRh$) [17] $BacNa_V$s revealed electron density spanning from the beginning of the transmembrane segment S5 (Ile150) through the end of the cytoplasmic coiled-coil domain (Ser285) (Fig. S1a). $Na_VAe1p$ shows the funnel-shaped architecture found in other $BacNa_V$s [15–17,20] (Fig. 1a and b). Each tetramer subunit is composed of S5 and S6 transmembrane helices that form the outer and inner parts of the PD, respectively. The P1 and P2 pore helices bridge S5 and S6 and are connected by the selectivity filter (Fig. 1).

Initial electron density maps (Fig. S1a) revealed an element absent from prior $BacNa_V$ structures, a long helical cytoplasmic tail (Figs. 1a and 2a). The $Na_VAe1p$ tetramer forms the asymmetric unit and is packed in the crystal lattice such that the crystallographic axes are not coincident with the channel 4-fold symmetry axis (Fig. S1b and Table S1). This arrangement leads to four, independent but similar channel protomers arranged around the channel central axis in the asymmetric unit. Model building and refinement ($R_{work}/R_{free}$ of 22.4/26.8; Table S1) showed that the pore-lining S6 helix continues for one turn after Met241, the intracellular pore constriction point (Fig. 2a). A 40° bend at His245 follows and leads to a continuous helix that terminates with a four-stranded, parallel coiled coil encompassing residues Leu265–Ser285 (Table S2). The clear quality differences between electron density maps calculated using data resolution cutoffs based on traditional (Fig. S1c) *versus* $CC_{1/2}$ metrics (Fig. S1d) support the choice of resolution cutoff based on $CC_{1/2}$ values. The obvious differences in map quality reinforce the assertion that

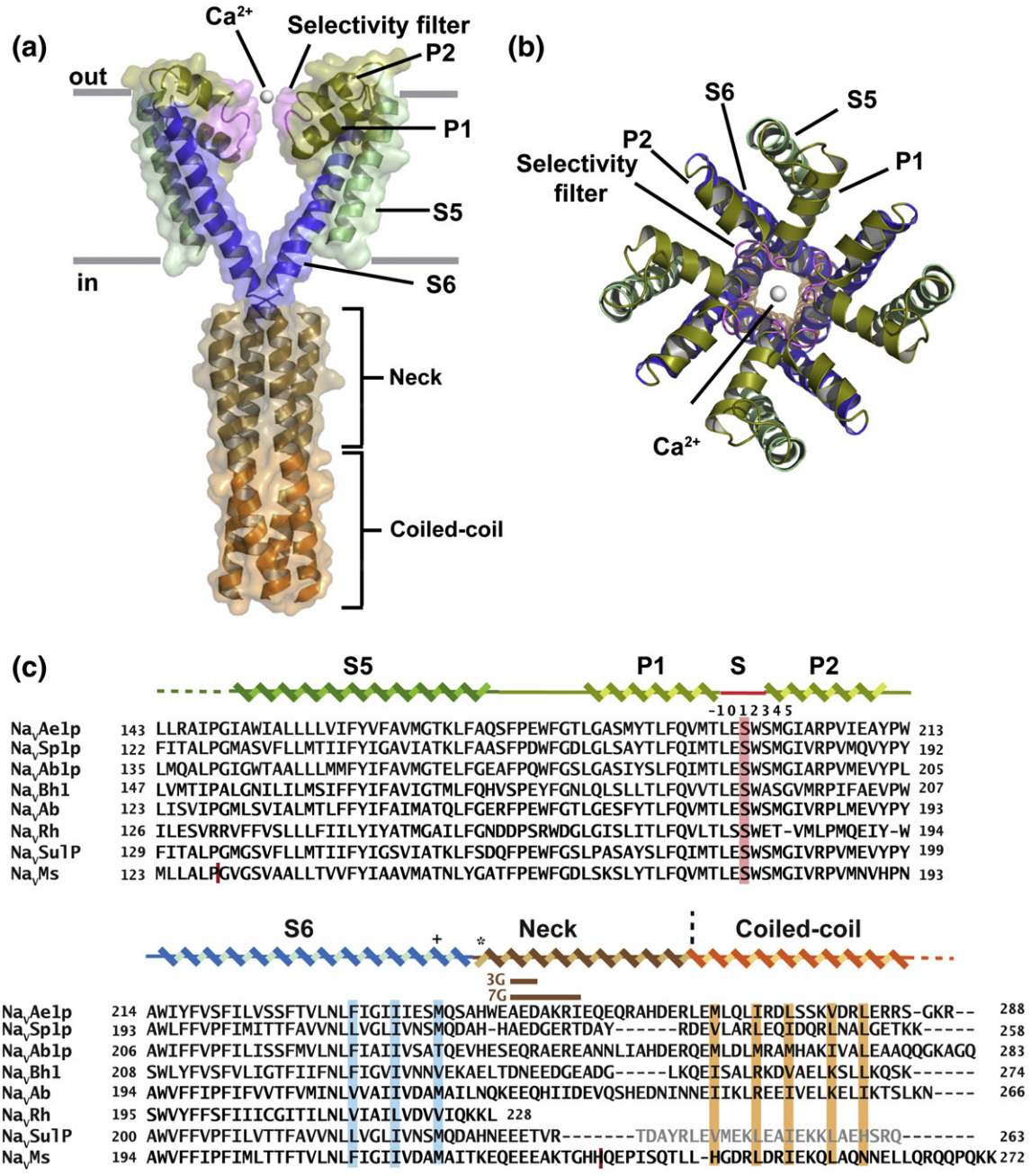


**Fig. 1.** Structure of the *A. ehrlichei* pore-only sodium channel protein $Na_VAe1p$. (a) Side view showing two transmembrane region subunits and four cytoplasmic tail subunits. Transmembrane helices S5 and S6 are colored green and blue, respectively. P1 and P2 pore helices are colored olive. Selectivity filter is violet. Neck and coiled coil are tan and orange, respectively. Calcium ion is a white sphere. Gray lines show approximate lipid bilayer boundaries. (b) $Na_VAe1p$ tetramer extracellular view. Colors are as in (a). (c) $Na_VAe1p$ secondary structure and alignment with $BacNa_V$ PD sequences. $Na_VAe1p$ secondary structure elements are indicated and colored as in (a). Selectivity filter position numbers are indicated relative to position "0", $Na_VAe1p$ Glu197. "+" indicates the activation gate residue. "*" indicates position of the $Na_VAe1p$ His245 bend. Black vertical broken line indicates division between "Neck" and "Coiled-coil". Colored bars indicate the following: selectivity filter (+1) position, red; S6 pore lining, blue; and coiled-coil core residues, orange. Positions of 3Gly and 7Gly neck mutants are indicated in brown. Gray letters show $Na_VSulP$ portion used in the NaK chimera [29]. Red vertical lines show crystallized $Na_VMs$ pore-only construct boundaries [20]. Other sequences are as follows: $Na_VSp1p$, *S. pomeroyi* [19]; $Na_VAb1p$, *Alcanivorax borkumensis* [19]; $Na_VBh1$ (NaChBac), *Bacillus halodurans* [11]; $Na_VAb$, *A. butzleri* (GI: 157737984) [15]; $Na_VRh$, *Rickettsia* sp. (GI: 262276647) [17]; $Na_VSulP$, *Sulfitobacter pontiacus* (GI: ZP_00961826.1) [29]; and $Na_VMs$, *Magnetococcus* sp. (UniProt ID A0L5S6) [20].

adherence to traditional metrics for defining resolution limits can result in the omission of useful diffraction data [37,38].

The cytoplasmic tail is considerably longer than the pore-forming region (~65 Å *versus* ~40 Å, respectively). Consequently, $Na_VAe1p$ spans ~110 Å in the axial dimension and resembles the general architecture of a NaK-$Na_VSulP$ chimera [29] and the full-length KcsA potassium channel [40] (Fig. 2b and c, respectively). The coiled coil is common among $BacNa_Vs$ [28] and is thought to participate in channel assembly [28,30]. Its location, C-terminal to a segment that trails S6, is reminiscent of similar domains from eukaryotic Kv7 (KCNQ) [41,42] and TRP channels

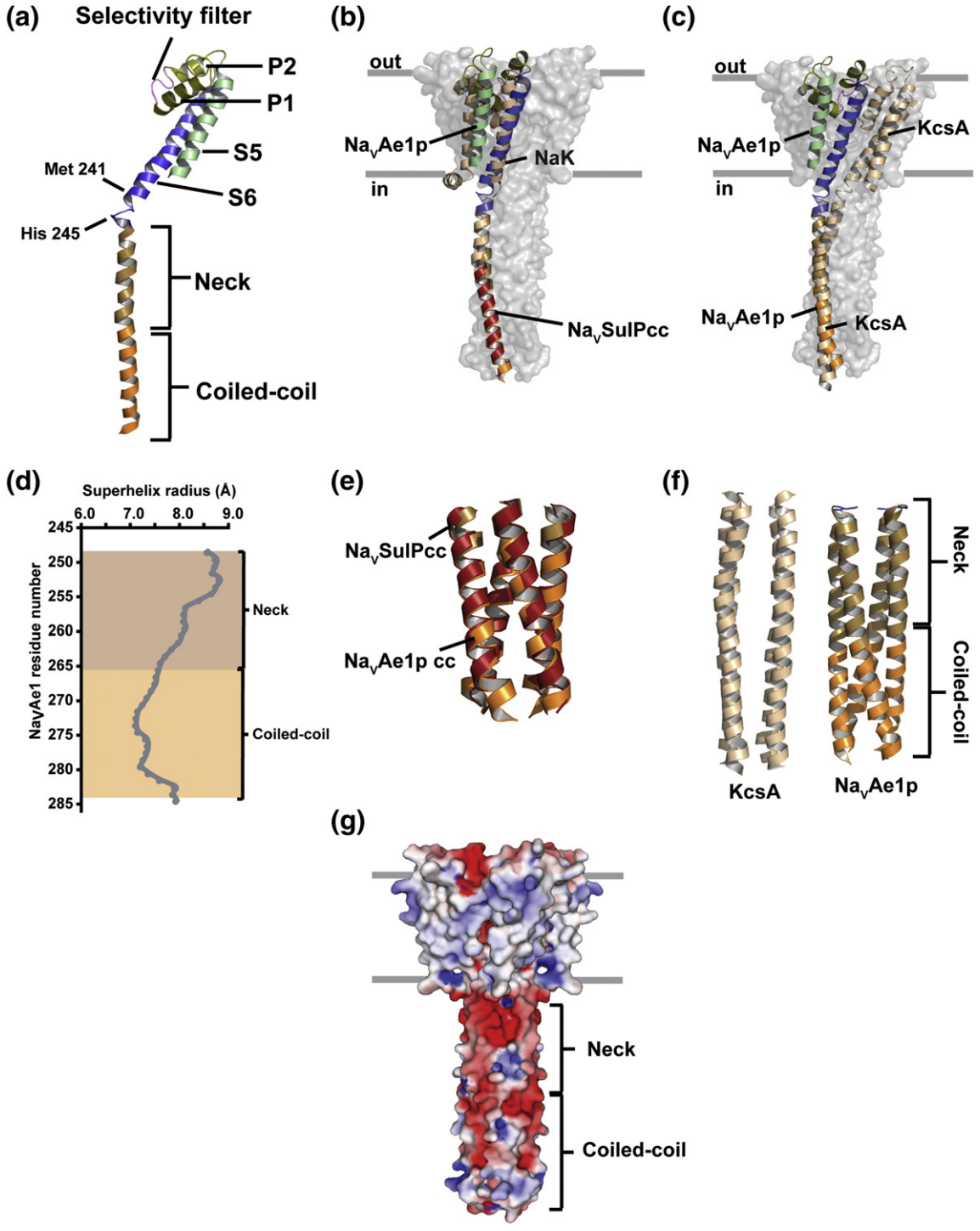

[43] and agrees with predictions [28] and a similar structure in the NaK-$Na_V$SulP chimera [29] (Fig. 2b).

The cytoplasmic tail arrangement resembles the stems of a flower bouquet. Individual helices interact extensively at the C-terminal base throughout the 18-residue coiled coil but splay apart above Met267 into individual helical stems that connect the coiled coil to S6 (Fig. 2d). This region, termed the "neck" (Figs. 1a and 2a), extends over six helical turns. The distance between the $C^{\alpha}$ positions and the superhelix axis widens from ~7 Å in the coiled coil to ~9 Å in the neck (Fig. 2d). The neck showed another unexpected feature, a large electron density that anomalous scattering indicated as a metal ion (Fig. S2a). *B*-Factors indicate that the neck is as well ordered as other parts of the structure with the exception of the region near the neck ion (Fig. S2b).

Comparison of $Na_V$Ae1p with a chimera between the nonselective NaK channel and the $BacNa_V$ $Na_V$SulP coiled coil [29] shows good agreement in the coiled coils (Fig. 2b and e and Table S3) (RMSD $C^{\alpha}$ = 1.2 Å for the tetramer). Contrastingly, the corresponding KcsA region, where there is no superhelical coil (Table S2), poorly matches the $Na_V$Ae1p coiled coil (Figs. 2c and f and Table S3) and reveals an unexpected diversity in how seemingly similar cytoplasmic domains can assemble. The essentially continuous helical conformation from S6 to the coiled coil is contrary to predictions from circular dichroism and sequence analysis suggesting that this $BacNa_V$ region is disordered [28]. Notably, the neck has an abundance of charged and polar residues (15/20 residues) (Figs. 1c and 2g). This density of hydrophilic residues may be important for neck function.

## Comparison of $Na_V$Ae1p pore region with other $BacNa_V$ structures

$Na_V$Ae1p conforms to expectations for a closed conformation as the selectivity filter is not collapsed and the intracellular gate is closed (Fig. 3a and b and Fig. S2c). Overall, the PD superposes well with other $BacNa_V$s (Fig. 3c and Table S3). Despite the VSD absence, S5 has position similar to that seen in $Na_V$Ab and is only substantially different from S5 of $Na_V$Rh, which is the outlier of currently known $BacNa_V$ structures. The main variations from other $BacNa_V$s lie in the C-terminal ends of S6 from the putative inactivated $Na_V$Ab conformation [16] and $Na_V$Ms pore [20] (Fig. 3c and Fig. S3).

$Na_V$Ae1p has a wide extracellular funnel that connects through the selectivity filter to the central cavity (Fig. 3a). Side-chain oxygens of selectivity filter residue Ser198 form the narrowest extracellular constriction (pore radius, 1.6 Å) (Fig. 3b). This is larger than that seen at the analogous $Na_V$Rh position (pore radius, 1.1 Å), where the filter is closed [17], but is not as wide as that in $Na_V$Ab (pore radius, 2.3 Å) [15] (Fig. 3b and Fig. S4). It is important to point out that the structure of $Na_V$Ms has a diameter that is close to that of the other $BacNa_V$s (Fig. 3b) due to the similarity of its backbone positions with the other $BacNa_V$ structures (Table S3). The remaining differences for $Na_V$Ms are largely due to the fact that the $Na_V$Ms structure has incomplete side chains at seven out of eight of the positions that correspond to the $Na_V$Ae1p residues that constrict the inner cavity, Phe233 and Ile237 (Fig. 3a), and it truncates in three of the subunits before the portion that corresponds to $Na_V$Ae1p Met241. The inner diameter of all of the solved structures contrasts to that of the open state model $Na_V Ms_{OM}$ that is generated from the most deviant subunit in the $Na_V$Ms structure (Fig. 3b) [20].

The inside of the selectivity filter abuts an aqueous cavity that includes lateral openings to the membrane and that ends in a constriction formed by S6 residues Phe223, Ile237, and Met241 (Fig. 3a and b), positions largely conserved among $BacNa_V$s (Fig. 1c). Both the presence of $F_o - F_c$ electron density (Fig. 3d) and a side-chain sulfur difference anomalous signal (Fig. S2a) support the placement of Met241 as the site of intracellular pore closure. This position corresponds to the suggested $Na_V$Ab activation gate [15] and, strikingly, forms a closure point further along S6 than in all but the initial $Na_V$Ab structure (Fig. 2b). It is notable that evaluation of possible boundaries of the lipid bilayer hydrophobic portion [45] suggests that, unlike other $BacNa_V$ structures, the $Na_V$Ae1p activation gate region protrudes from the bilayer core into the zone comprising phospholipid head groups (Fig. S5).

**Fig. 2.** $Na_V$Ae1p structure comparison and analysis. (a) Side view of a single $Na_V$Ae1p monomer. Secondary structure elements are labeled and colored as in Fig. 1. Select residue positions are indicated. (b) $C^{\alpha}$ superposition of the tetrameric $Na_V$SulP region of the NaK-$Na_V$SulP chimera [29] ($Na_V$SulP portion, red; NaK portion, wheat) with equivalent parts of the $Na_V$Ae1p neck and coiled coil (colored as in Fig. 1). One $Na_V$Ae1p and NaK-$Na_V$SulP chimera monomer is shown in cartoon representation in front of the surface of three remaining $Na_V$Ae1p subunits. (c) $C^{\alpha}$ superposition of the $Na_V$Ae1p coiled-coil tetramer with the equivalent KcsA residues. One $Na_V$Ae1p (colored as in Fig. 1) and KcsA (wheat) monomer is shown in cartoon representation in front of the surface of three remaining $Na_V$Ae1p subunits. (d) Plot of $Na_V$Ae1p coiled-coil superhelix radius *versus* residue number. Neck and coiled-coil elements are shaded as in (a). (e) Close-up of the coiled-coil regions of $Na_V$Ae1p (orange) and $Na_V$SulP (red) used for superposition in (b). (f) Close-up of the cytoplasmic parts of KcsA (left panel, wheat) and $Na_V$Ae1p (neck, sand; coiled coil, orange). (g) $Na_V$Ae1p electrostatic surface potential [$+4kT$ (blue) to $-4kT$ (red)] mapped on the channel van der Waals surface. Gray lines show approximate lipid bilayer boundaries.

### Identification of the "outer ion" binding site

We found a large positive electron density peak perched on the 4-fold axis of the channel at the selectivity filter outer mouth (Fig. 3e). Calculation of anomalous difference maps at 6.5 Å revealed a strong peak (11σ) indicating the presence of a non-protein anomalous scatterer (Fig. 3f and Fig. S6a–d). Recognizing that there could be challenges in identifying this peak due to the data resolution, we searched for other evidence that it represented an ion and not noise or some other possibility. We found a similar non-protein anomalous scatterer at the exact same location in a second lower-resolution (3.80 Å) data set ($Na_VAe1p$, crystal II; Table S1 and Fig. S6c) obtained from a crystal grown using the same high-calcium (200 mM $CaCl_2$) conditions as the crystal that yielded the 3.46-Å-resolution data set. By contrast, there was no anomalous peak at this location in maps calculated from crystals grown

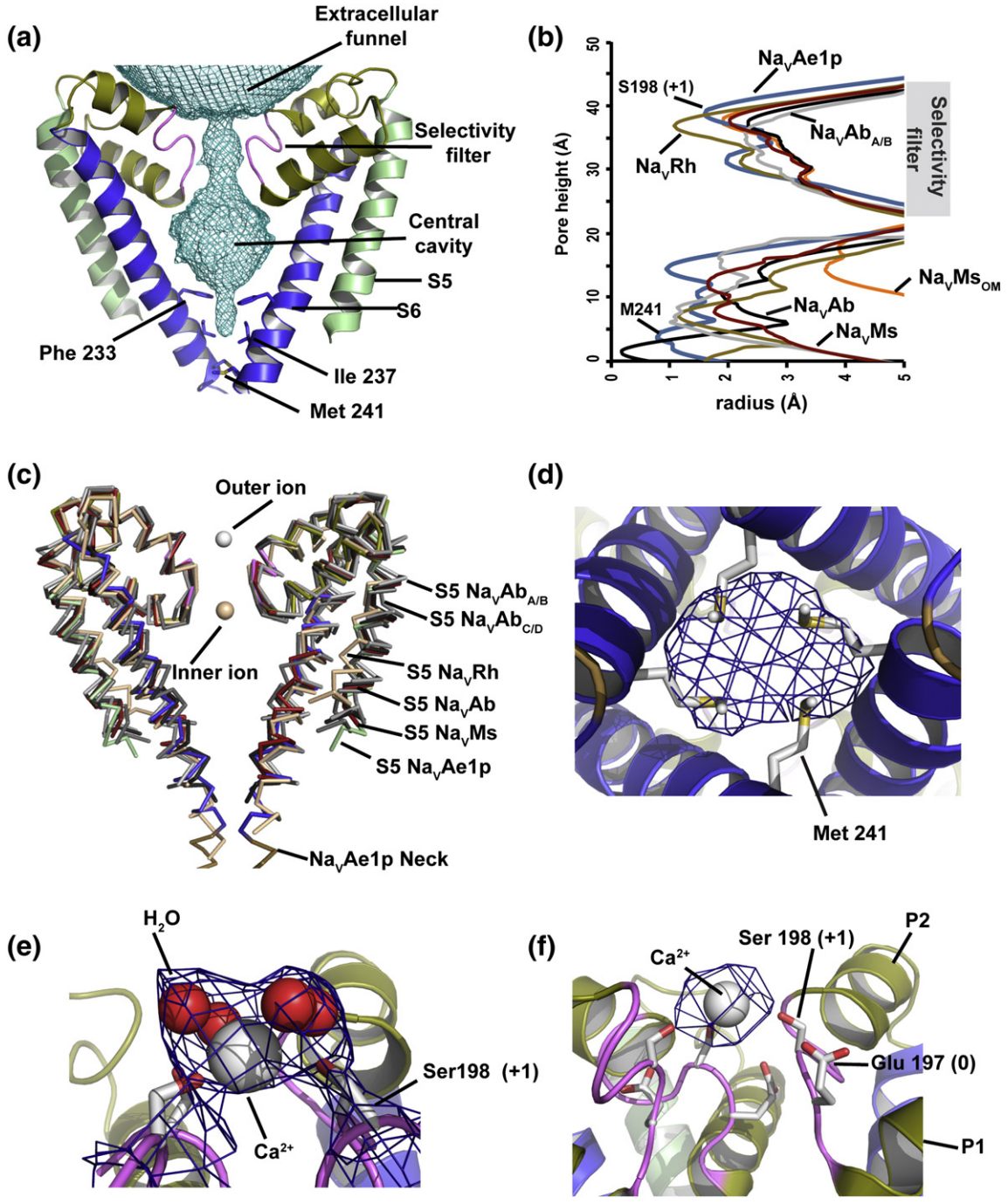

without calcium (Figs. S1e and S6c). In all three cases, the maps, which are all calculated at the same resolution (6.5 Å), showed strong evidence for the neck ion. Finally, structural studies of the H245G mutant, in which crystals were grown in the absence of calcium and in the identical space group as $Na_VAe1p$ crystal I and crystal II (Fig. S6c), gave no evidence for the selectivity filter ion. Given these multiple lines of evidence that the anomalous peak at the selectivity filter outer mouth depends on the presence of calcium, we assigned this density as a calcium ion.

Inclusion of the ion alone in the refinement left substantial unaccounted electron density. Taking into account the ion position and likelihood that it is partly solvated, we modeled four waters using standard calcium coordination geometry (Fig. 3e). We also found additional positive difference ($F_o - F_c$) electron density extending from the outer ion position through the selectivity filter along the 4-fold channel axis; however, we were unable to model whether this arises from ions or solvent (Fig. S6e). The refined structure shows a partially hydrated calcium ion coordinated by four $Na_VAe1p$ serine oxygens and four water molecules, giving a coordination number common to protein–$Ca^{2+}$ complexes [46] and serine oxygen–$Ca^{2+}$ distances (2.9–3.5 Å) that are within those for calcium ions partially coordinated by protein ligands [46,47].

We denote the calcium ion position as the "outer ion" because it is separated from the previously reported selectivity filter inner ion position [17,35] by 10.7 Å (Fig. 3c). The outer ion site also does not correspond to the position of the unassigned selectivity filter density reported for $Na_VMs$ [20]. Observation of the outer ion binding site, together with the strong structural (Fig. 3c) and sequence similarity (Fig. 1c) of the region and previous identification of an inner ion site, establishes that $BacNa_V$ selectivity filters have more than one ion binding site. Sodium and calcium ions have similar radii (0.95 Å *versus* 0.99 Å, respectively) and coordination geometries [2]. Hence, the outer ion position appears to mark the site of entry and partial dehydration as the ion passes into the selectivity filter.

To facilitate comparison among $Na_V$, $Ca_V$, and $BacNa_V$ selectivity filters, we denote the residue corresponding to the mammalian $Na_V$ "DEKA" motif [2] and the conserved glutamates in $Ca_V$s [2,33] and $BacNa_V$s (Fig. 1c) as position "0". Other residues are numbered positively or negatively relative to this residue (Fig. 4a). Hence, the $Na_VAe1p$ Ser198 (+1) side-chain oxygens coordinate the outer ion (Fig. 3e). Comparison of $BacNa_V$ and $Ca_V$ selectivity filter sequences revealed that the (+1) position is strictly conserved as an acidic residue in $Ca_V$ domain II selectivity filters (Fig. 4b). This (+1) position had not been previously implicated in $Ca_V$ selectivity. As it plays a role in $BacNa_V$ calcium selectivity [19,48], the compelling similarities together with the observation of a bound calcium ion prompted us to examine the role of the (+1) position in a mammalian $Ca_V$.

## Outer ion site is important for mammalian $Ca_V$ ion binding

Calcium selectivity in $Ca_V$s is thought to arise from the interaction of permeant calcium ions with a ring of selectivity filter (0) position glutamates [33,49]. Following experiments that first demonstrated the importance of the (0) position glutamates [33], we used two-electrode voltage clamp to measure calcium block of lithium currents through human cardiac $Ca_V1.2$ channels expressed in *Xenopus* oocytes and examined how (+1) position mutations in domain II affect the high-affinity calcium site. In contrast to previous reports [33], we found that D707N channels exhibited a reduction in the apparent calcium affinity relative to wild type ($IC_{50}$, 11.3 ± 2.0 μM and 1.9 ± 0.2 μM for D707N and wild type, respectively) (Fig. 4c and d). This change was equivalent to that caused by the charge neutralization E1115Q ($IC_{50}$, 15.1 ± 1.9 μM), the (0) position glutamate neutralization having the largest reported impact on the high-affinity site [33,49]. Changing D707 to alanine to mimic the corresponding $Ca_V$ domain IV position caused a reduction in apparent affinity similar to D707N ($IC_{50}$, 13.6 ± 2.1 μM). Complete removal of the D707 side chain by D707G to mimic the equivalent position of $Ca_V$ domains I and III caused an even greater

**Fig. 3.** $Na_VAe1p$ pore region analysis. (a) $Na_VAe1p$ pore volume represented as a teal mesh calculated by CAVER [44]. In order to show the central cavity, dummy atoms closed the side vestibules. S6 residues forming the narrow constriction are shown as sticks and labeled. $Na_VAe1p$ elements are labeled as in Fig. 1. (b) Plot of channel radius *versus* distance along the central channel axis for closed $Na_VAb$ [15] (black), inactivated $Na_VAb_{A/B}$ [16] (light gray), $Na_VRh$ [17] (wheat), $Na_VMs$ (dark red) [20], $Na_VMs_{OM}$ (orange) open state model following [20], and $Na_VAe1p$ (blue). $Na_VAe1p$ constriction points caused by selectivity filter residue Ser198 and S6 residue Met241 are indicated. (c) Backbone superposition of PDs of $Na_VAb$ [15] (black), $Na_VAb_{A/B}$ [16] (light gray), $Na_VAb_{C/D}$ [16] (medium gray), $Na_VRh$ [17] (wheat), $Na_VMs$ [20] (dark red), and $Na_VAe1p$ [colored as in (a)]. Outer ion from $Na_VAe1p$ and inner ion from $Na_VRh$ are shown as white and wheat spheres, respectively. Two subunits are shown. (d) View from the intracellular side showing M241 side-chain $F_o - F_c$ density. (e) Outer ion site side view. $Ca^{2+}$ (white sphere) is surrounded by four water molecules (red spheres), and Ser198 (+1) is shown in sticks with $2F_o - F_c$ density surrounding the $Ca^{2+}$ ion as a 1.0σ contoured blue mesh. (f) Side view of outer ion anomalous difference density (blue mesh) calculated at 6.5 Å and contoured at 6.5σ. Glu197 (0) and Ser198 (+1) are indicated. $Ca^{2+}$ is shown as a white sphere. The front channel monomer is removed for clarity.

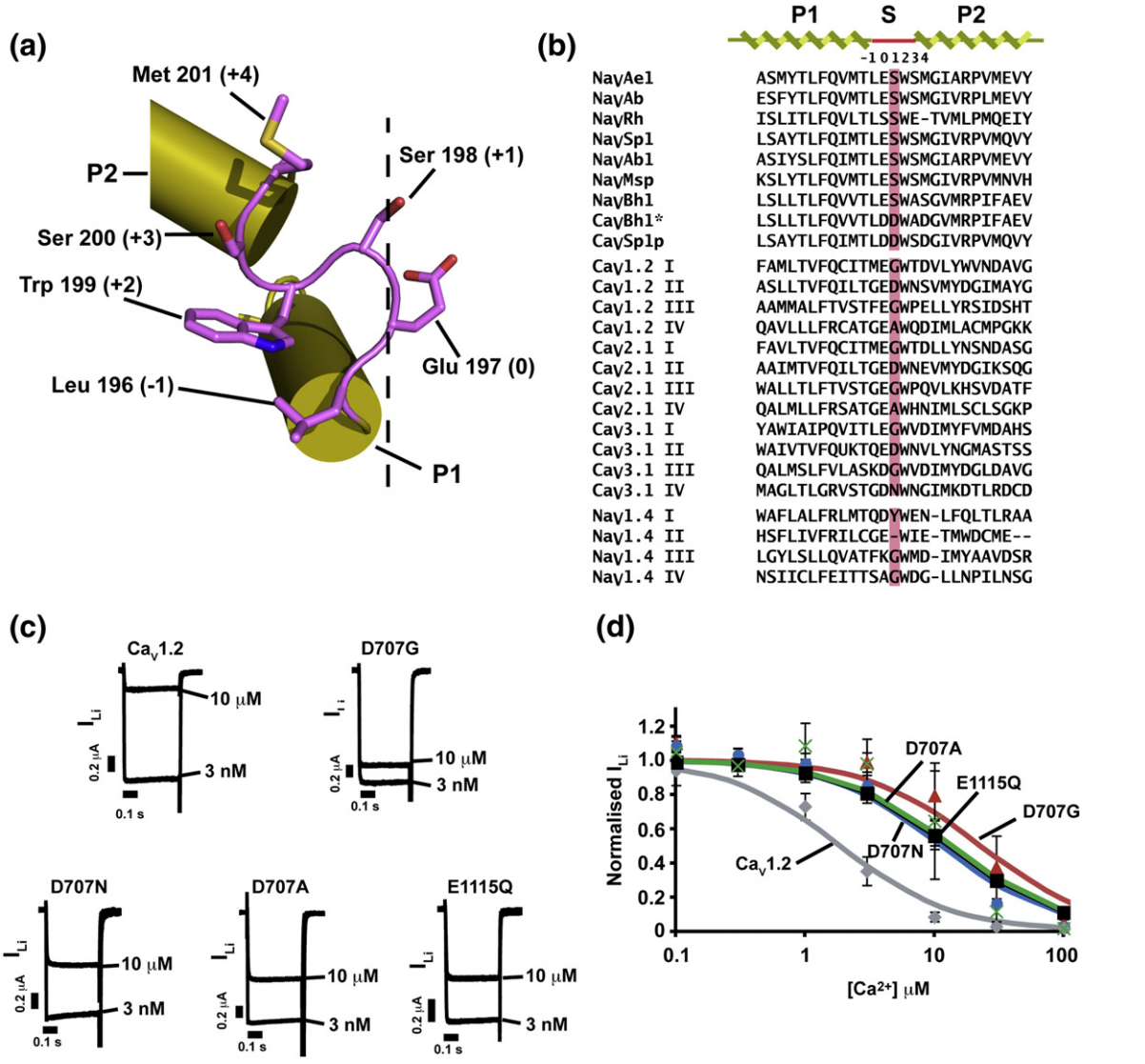


**Fig. 4.** Selectivity filter (+1) position is conserved in mammalian $Ca_V$s and important for ion binding. (a) Cartoon depiction of a single $Na_V$Ae1p subunit selectivity filter colored as in Fig. 1. Selectivity filter residues are shown and indicated relative to the (0) position glutamate. Broken line shows the central pore axis approximate position. (b) Selectivity filter and pore helices sequence alignment for selected BacNa$_V$s, mammalian $Ca_V$ subtype exemplars, and mammalian $Na_V$1.4. $Ca_V$Bh1 and $Ca_V$Sp1p are calcium selective mutants of $Na_V$Bh1 (NaChBac) [48] and $Na_V$Sp1p [19], respectively. Selectivity filter numbering is indicated. (c) Two-electrode voltage-clamp recordings from *Xenopus* oocyte expressing wild-type $Ca_V$1.2 or the indicated mutants recorded in a buffer containing 100 mM $Li^+$ and either 3 nM or 10 μM free $Ca^{2+}$ and normalized to the 3-nM trace. Currents were elicited by a voltage step from −90 mV to −20 mV. (d) Dose–response curves for calcium block of lithium currents for $Ca_V$1.2 (gray), E1115Q (black), D707N (blue), D707A (green), and D707G (red). Each data point at each calcium concentration is normalized to the current at 3 nM $Ca^{2+}$ and averaged for $n$ = 5–7 oocytes. Error bars are standard error of the mean.

reduction in calcium binding ($IC_{50}$, 22.8 ± 6.7 μM). The magnitude of the effects of the D707 neutralizations are striking, as this position is much more exposed to bulk solvent than the (0) position glutamate, and strongly suggest that the effects of the D707 mutation are through direct interaction with $Ca^{2+}$ rather than a indirect consequence of electrostatic environment alteration. These data demonstrate the importance of a previously unrecognized calcium binding determinant of mammalian $Ca_V$s. These findings underscore the similarities between selectivity filters of homomeric Bac$Na_V$s and their more distant eukaryotic relatives, which have four nonidentical selectivity filter repeats.

### S6 activation gate residue and neck are important for BacNa$_V$ gating

Observation of a complete BacNa$_V$ cytoplasmic domain connected to a closed pore prompted us to test how the newly described channel elements (Fig. 5a) contribute to function. In line with the low success rate of BacNa$_V$ functional expression [12,17], our initial attempts to measure currents from full-length Na$_V$Ae1 using transfected mammalian cells or mRNA injected *Xenopus* oocytes failed. Therefore, we turned to Na$_V$Sp1, a previously characterized *Silicibacter pomeroyi* homolog [12] (Figs. 1c and 5b).

As prior structural studies have not achieved consensus regarding which S6 residues close the intracellular side of the pore (Fig. 3b), we first examined the Na$_V$Sp1 S6 positions equivalent to those that narrow the Na$_V$Ae1p intracellular side (Fig. 3a). Alanine substitution in each of the two helical turns above the constriction site, Na$_V$Ae1p F233 and I237 (Na$_V$Sp1 L212A and I216A) (Figs. 3a and 5a and Fig. S7a), did not affect the voltage dependence of activation ($V_{1/2,act}$) ($\Delta V_{1/2,act} = -1.0 \pm 4.5$ and $-0.4 \pm 4.8$ mV, respectively) (Fig. 5c and Table 1). However, these mutants did shift the voltage dependence of inactivation ($V_{1/2,inact}$) to more negative potentials ($\Delta V_{1/2,inact} = -14.8 \pm 4.3$ and $-14.0 \pm 3.8$ mV, respectively) (Fig. 5c and Table 1), decreased the inactivation time constants, and accelerated recovery from inactivation (Fig. S7b and c). By contrast, alanine substitution of the position equivalent to the pore occlusion point, Na$_V$Ae1p Met241 (Na$_V$Sp1, M220A) (Figs. 3a and 5a), caused dramatic negative shifts in both $V_{1/2,act}$ and $V_{1/2,inact}$ ($\Delta V_{1/2,act} = -49.8 \pm 3.3$ mV and $\Delta V_{1/2,inact} = -40.0 \pm 3.5$ mV) (Fig. 5d and Table 1) but left the inactivation time constants and recovery from inactivation unaltered (Fig. S7b and c). The major effect of Na$_V$Sp1 M220A on $V_{1/2,act}$ contrasted against the absence of $V_{1/2,act}$ changes from mutation of residues further into the central cavity suggests a critical role for this position in stabilizing the closed state of the channel and indicates that the more distal positions are important for inactivation only.

Because of its direct structural connection to the activation gate, we next examined how the helical structure of the neck affected channel behavior by using a strategy of glycine substitutions to destabilize the helical conformation [50–52]. Because BacNa$_V$ necks have variable lengths, we focused on the most conserved region (Fig. 1c). Similar to the S6 mutant Na$_V$Sp1 M220A, single-glycine substitutions at each of the three residues below the bend Na$_V$Ae1p Ala248, Glu249, Asp250 (Na$_V$Sp1, A226G, E227G, and D228G) caused a significant negative shift in $V_{1/2,act}$ (Fig. 5e, Table 1, and Fig. S7d and e). By contrast, alanine substitutions at Na$_V$Sp1 E227 and D228 yielded essentially wild-type channels (Fig. 5e, Table 1, and Fig. S7d and e), indicating that the glycine impact comes from increased flexibility rather than side-chain deletion. Increasing the consecutive numbers of Na$_V$Sp1 neck glycines to two (residues 227–228), three (residues 226–228), and seven (residues 226–232) further facilitated activation gate opening that was coupled to negative shifts in $V_{1/2,inact}$ ($\Delta V_{1/2,act} = -25.3 \pm 2.6$, $-35.0 \pm 3.8$, and $-40.7 \pm 3.9$ mV and $\Delta V_{1/2,inact} = -4.5 \pm 3.2$, $-18.1 \pm 3.6$, and $-22.1 \pm 5.2$ mV for 2Gly, 3Gly, and 7Gly, respectively) (Fig. 5e and f and Table 1). The 2Ala mutant revealed that part of the shift caused by the 2Gly mutant arises from a synergistic effect of removing Na$_V$Sp1 E227 and D228 simultaneously [$\Delta V_{1/2,act} = -15.7 \pm 3.4$ *versus* $-25.3 \pm 2.6$ mV for 2Ala and 2Gly, respectively (Fig. 5e and Table 1)], which indicates an additional role for these charges. Nevertheless, the 7Ala mutant had activation properties similar to wild type and that strongly contrasted the large negative shifts in $V_{1/2,act}$ and $V_{1/2,inact}$ caused by 7Gly ($\Delta V_{1/2,act} = 4.7 \pm 4.4$ *versus* $-40.7 \pm 3.9$ mV for 7Ala and 7Gly, respectively). The major negative shifts in $V_{1/2,act}$ produced by neck substitutions that are detrimental to helix formation strongly support the idea that a structured neck is critical for closed state stabilization.

The majority of neck mutants causing negative shifts in $V_{1/2,act}$ also elicited negative shifts in $V_{1/2,inact}$ (Fig. 5e and Table 1). However, unlike previously reported mutations in the Na$_V$SulP coiled coil that slowed $\tau_{inact}$ by an order of magnitude or more [29], most of the neck mutants left $\tau_{inact}$ unperturbed (Fig. S7f and g). Of the few that did not (E227G, D228G, 2G, and 7G; $P < 0.001$), none caused a perturbation larger than a factor of three. To examine this discrepancy further, we characterized Na$_V$Sp1 R242E (Fig. S8), a substitution at a conserved position at the N-terminal end of the coiled-coil region that was reported to cause a negative shift in $V_{1/2,act}$ and slow Na$_V$SulP inactivation by ~37-fold [29]. Although Na$_V$Sp1 R242E did cause a negative shift in $V_{1/2,act}$ (Table 1), unlike its Na$_V$SulP counterpart, this change caused only a modest (~2.7-fold, $P = 0.04$) slowing of inactivation (Fig. S8d).

Finally, we tested the consequences of alanine and glycine substitutions at the bend, Na$_V$Ae1p His245 (Na$_V$Sp1, H224) (Fig. 5g and Fig. S9a). Na$_V$Sp1 H224A did not affect $V_{1/2,act}$ or $V_{1/2,inact}$ ($\Delta V_{1/2,act} = 2.8 \pm 4.2$ and $\Delta V_{1/2,inact} = -5.4 \pm 4.8$ mV) (Fig. 5g and Table 1) but did slow inactivation (~2-fold, $P < 0.001$) (Fig. S9b). In contrast, Na$_V$Sp1 H224G spared $V_{1/2,act}$ and caused a large negative shift in $V_{1/2,inact}$ ($\Delta V_{1/2,act} = -4.5 \pm 3.9$ mV and $\Delta V_{1/2,inact} = -25.0 \pm 4.0$ mV) (Fig. 5g and Table 1). Although local disorder (Fig. S2b) precluded us from modeling the Na$_V$Ae1p His245 side chain, this residue could coordinate the neck ion. To test the structural consequence of loss of this potential ligand, we determined a 5.8 Å-resolution structure of Na$_V$Ae1p H245G crystallized from a

low-calcium condition (Table S1). The structure showed no major changes from wild type except for the loss of anomalous density for the neck ion and outer ion (Fig. S8c) (RMSD $C^{\alpha}$ = 0.5 Å for the tetramer relative to wild type). Hence, the bend residue appears to be important for neck ion coordination but the neck ion is not essential for the bend structure or helical character of the neck.

Our structure-based mutational studies uncovered two functional phenotypes. Mutations in the activation gate and neck having negative shifts in $V_{1/2,act} \geq -20$ mV also caused negative shifts in $V_{1/2,inact}$, suggesting that the two processes are strongly coupled. Mutations at S6 residues above the activation gate and bend residue H224 selectively impacted $V_{1/2,inact}$ (Table 1). Together, these data support the ideas that (i) the $Na_VAe1p$ structure represents a closed state, (ii) destabilization of the neck facilitates channel opening, and (iii) residues in S6 above the constriction site and at the bend are important for the molecular transitions underlying inactivation.

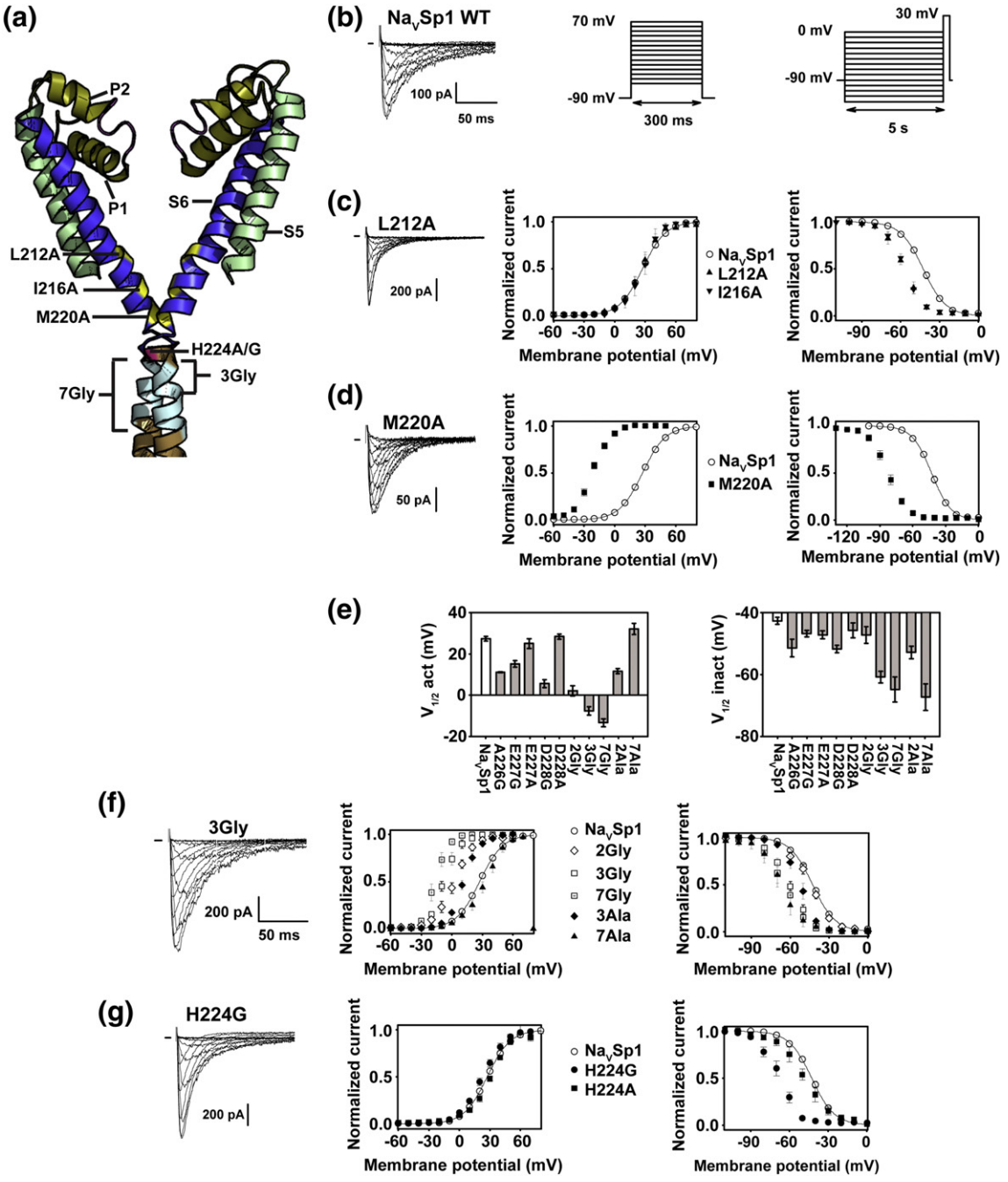

**Table 1.** Activation and inactivation properties of BacNa$_V$s and mutants

| | $V_{1/2,act}$ | $\Delta V_{1/2,act}$ | *n* | *P*-Value | $V_{1/2,inact}$ | $\Delta V_{1/2,inact}$ | *n* | *P*-Value |
|---|---|---|---|---|---|---|---|---|
| Na$_V$Sp1 | 27.4 ± 1.1 | — | 13 | n.a. | −42.7 ± 1.1 | — | 12 | n.a. |
| S6 | | | | | | | | |
| L212A | 26.4 ± 3.1 | −1.0 ± 4.5 | 5 | n.s. | −57.5 ± 2.7 | −14.8 ± 4.3 | 6 | *** |
| I216A | 27.0 ± 3.4 | −0.4 ± 4.8 | 3 | n.s. | −56.7 ± 1.6 | −14.0 ± 3.8 | 4 | *** |
| M220A | −22.4 ± 1.6 | −49.8 ± 3.3 | 7 | *** | −82.7 ± 1.8 | −40.0 ± 3.5 | 7 | *** |
| Bend | | | | | | | | |
| H224A | 30.2 ± 1.1 | 2.8 ± 4.2 | 3 | n.s. | −48.1 ± 3.5 | −5.4 ± 4.8 | 3 | n.s. |
| H224G | 22.9 ± 1.7 | −4.5 ± 3.9 | 4 | n.s. | −67.7 ± 2.3 | −25.0 ± 4.0 | 4 | *** |
| Neck | | | | | | | | |
| A226G | 11.1 ± 0.2 | −16.3 ± 4.2 | 3 | *** | −51.4 ± 2.8 | −8.7 ± 4.3 | 4 | *** |
| E227G | 15.2 ± 1.5 | −12.2 ± 3.3 | 6 | *** | −46.8 ± 1.1 | −4.1 ± 3.6 | 4 | n.s. |
| E227A | 25.1 ± 2.3 | −2.3 ± 4.1 | 4 | n.s. | −47.1 ± 1.3 | −4.4 ± 3.2 | 6 | * |
| D228G | 5.7 ± 1.9 | −21.7 ± 3.9 | 4 | *** | −51.7 ± 1.2 | −9.0 ± 3.6 | 4 | *** |
| D228A | 28.4 ± 1.3 | 1.0 ± 4.3 | 3 | n.s. | −45.7 ± 2.5 | −3.0 ± 4.2 | 4 | n.s. |
| 2G | 2.1 ± 2.4 | −25.3 ± 2.6 | 6 | *** | −47.2 ± 2.6 | −4.5 ± 3.2 | 4 | n.s. |
| 2A | 11.7 ± 1.3 | −15.7 ± 3.4 | 5 | *** | −52.8 ± 2.0 | −10.1 ± 3.9 | 4 | *** |
| 3G | −7.6 ± 2.1 | −35.0 ± 3.8 | 5 | *** | −60.8 ± 1.9 | −18.1 ± 3.6 | 10 | *** |
| 7G | −13.3 ± 1.9 | −40.7 ± 3.9 | 4 | *** | −64.8 ± 4.1 | −22.1 ± 5.2 | 4 | *** |
| 7A | 32.1 ± 2.8 | 4.7 ± 4.4 | 4 | n.s. | −67.3 ± 4.2 | −24.6 ± 5.2 | 4 | *** |
| Coiled coil | | | | | | | | |
| R242E | 7.8 ± 0.8 | −19.6 ± 3.3 | 5 | *** | −44.4 ± 2.5 | −1.7 ± 4.2 | 4 | n.s. |
| Na$_V$Ae1 | | | | | | | | |
| 3G | 32.1 ± 1.1 | n.a. | 6 | | 5.3 ± 3.1 | | 4 | |

Data are mean ± standard error of the mean.
$\Delta V_{1/2}$ "±" denotes 90% confidence interval.
*P*-Values are calculated relative to wild-type Na$_V$Sp1.
n.s., not significant; $P > 0.05$.
"*" indicates $0.001 < P < 0.05$.
"***" indicates $P < 0.001$.

## Neck destabilization allows Na$_V$Ae1 functional characterization

Having established the importance of the neck helical structure for closed state stabilization, we revisited Na$_V$Ae1 functional studies to test whether glycine substitution in the neck would permit us to record from full-length channels. Indeed, Na$_V$Ae1 channels bearing the 3Gly mutation (residues 248–250) produced voltage-dependent channels (Fig. 6a and b). These had a $V_{1/2,act}$ similar to Na$_V$Sp1 but ~40 mV more positive than the equivalent Na$_V$Sp1 3Gly mutant ($V_{1/2,act}$ = 32.1 ± 2.8, 27.4 ± 1.1, and −7.6 ± 2.1 mV for Na$_V$Ae1 3Gly, Na$_V$Sp1, and Na$_V$Sp1 3Gly, respectively). These results further support the idea that the neck helical structure is important for closed state stabilization and suggest that wild-type Na$_V$Ae1 has a very positive $V_{1/2,act}$ of activation that had prevented functional characterization.

The ability to record from Na$_V$Ae1 3Gly allowed us to test the functional properties of the Na$_V$Ae1 selectivity

**Fig. 5.** Functional studies of Na$_V$Sp1 structure-based mutants. (a) Na$_V$Ae1p cartoon depicting positions investigated by patch-clamp. S6, bend, and neck positions are colored yellow, red, and light blue, respectively, and are indicated using the corresponding Na$_V$Sp1 residues. (b) Left panel, exemplar Na$_V$Sp1 $Na^+$ currents in response to the activation protocol shown in the middle panel (300 ms depolarizations from −60 to +70 mV in 10 mV steps from a holding potential of −90 mV, sweep-to-sweep interval = 5 s). Right panel, protocol for examining steady-state inactivation voltage dependence (5 s pre-pulse depolarization from 0 to −130 mV in 10 mV steps, followed by a 300-ms step to +30 mV, and repolarization to the holding potential, −90 mV; sweep-to-sweep interval = 10 s). (c) Left panel, exemplar Na$_V$Sp1 L212A $Na^+$ currents. Activation (middle panel) and inactivation (right panel) curves of Na$_V$Sp1 (open circles), L212A (black triangle), and I216A (inverted black triangle). (d) Left panel, exemplar Na$_V$Sp1 M220A $Na^+$ currents. Activation (middle panel) and inactivation (right panel) curves of Na$_V$Sp1 (open circles) and M220A (black squares). (e) $V_{1/2,act}$ and $V_{1/2,inact}$ for Na$_V$Sp1 and indicated neck mutants. (f) Left panel, exemplar Na$_V$Sp1 3Gly $Na^+$ currents. Activation (middle panel) and inactivation (right panel) curves of Na$_V$Sp1 (open circles), 2Gly (open diamonds), 3Gly (open squares), 7Gly (filled open squares), 3Ala (black diamonds), and 7Ala (black triangles). (g) Left panel, exemplar Na$_V$Sp1 H224G $Na^+$ currents. Activation (middle panel) and inactivation (right panel) curves of NavSp1 (open circles), H224G (black circles), and H224A (black squares). Activation curves are obtained by normalizing maximal amplitudes divided by the driving force. Inactivation curves are obtained by normalizing maximum amplitudes upon second pulse. NavSp1 activation and inactivation curve Boltzmann fits are shown in (c), (d), (f), and (g).

filter defined by our structure. In agreement with the strong selectivity filter conservation (Fig. 1c), biionic recording experiments (Fig. 6c and d) showed that $Na_VAe1$ has selectivity properties similar to other $BacNa_Vs$ including $Na_VSp1p$ [19], the "pore-only" version of $Na_VSp1$ ($P_{Ca}/P_{Na}$ = 0.07 ± 0.02 and 0.08 ± 0.01 for $Na_VAe1$ 3Gly and $Na_VSp1p$, respectively), and $Na_VBh1$ (NaChBac) [47]. Due to the relatively low current amplitude of $Na_VAe1$ 3Gly, we were restricted to this extrapolation method of examining the permeability ratio. Hence, we validated the measurement by determining the ion selectivity of full-length $Na_VSp1$ 3Gly, which expresses much better than $Na_VAe1$ 3Gly, by two methods, the extrapolation method used to examine $Na_VAe1$ 3Gly and a tail current protocol (Fig. S10). Both methods gave the same $P_{Ca}/P_{Na}$ ratio (0.05 ± 0.02 and 0.07 ± 0.02, respectively) and agree with the values for $Na_VAe1$ 3Gly and the "pore-only" $Na_VSp1p$. These results support the idea that the 3Gly mutation has minimal influence on selectivity and that $Na_VAe1$ is a sodium selective channel.

## Discussion

Structure determination of the "pore-only" $BacNa_V$ $Na_VAe1p$ revealed previously uncharacterized $BacNa_V$ architectural features that are important for function. The presence of the long helical intracellular domain allowed the complete definition of S6, which extends into the intracellular side of the membrane (Fig. S5). Relative to all but the initial $Na_VAb$ structure [15], which contained pore-lining cysteine mutants near the activation gate that may have influenced S6 positioning, this structure places the intracellular gate more toward the S6 C-terminus (Fig. 3b). It seems likely that the absence of a consensus among the prior $BacNa_V$ structures in defining the site of this important channel element arises from the fact that they lack the intracellular domain. The structural plasticity of the intracellular gate seems a likely consequence of it being the central point of structural changes required for gating and inactivation. Our observations are not unlike those described for KcsA in which the full-length structure [40] showed that the activation gate closure point was more intracellular than defined from a structure lacking the intracellular domain [53]. The $Na_VAe1p$ activation gate and subsequent helical extension of S6 should protrude beyond the boundaries of the hydrophobic portion of the lipid bilayer into the lipid head groups (Fig. S5). This location may have important consequences as, based on voltage-gated potassium channel studies [26], it could allow the C-terminal portion of S6 to interact directly with the phospholipid head groups in a way that could influence function. It might also permit

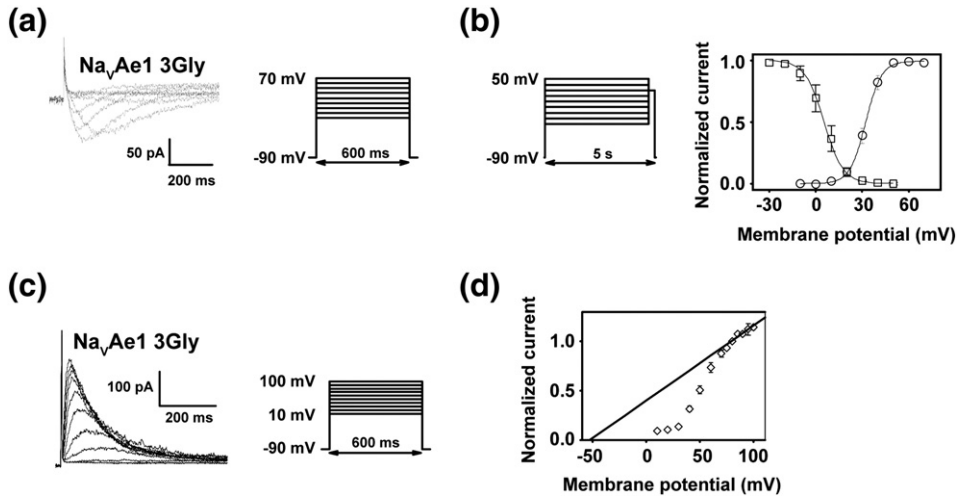


**Fig. 6.** $Na_VAe1$ functional properties. (a) Left panel, exemplar $Na_VAe1$ 3Gly $Na^+$ currents in response to an activation protocol, right panel (600 ms depolarizations from 0 to +70 mV in 10 mV steps from a holding potential of −90 mV, sweep-to-sweep interval = 5 s). (b) Left panel, protocol for examining steady-state inactivation voltage dependence (5 s pre-pulse depolarization from 50 to −30 mV in 10 mV steps, followed by a 300-ms step to + 30 mV, and repolarization to the holding potential, −90 mV; sweep-to-sweep interval = 10 s). Right panel, $Na_VAe1$ 3Gly activation and inactivation curves. Boltzmann fits are indicated. (c) Left panel, exemplar $Na_VAe1$ 3Gly currents in the presence of 130 mM intracellular $Na^+$ and 107.5 mM extracellular $Ca^{2+}$, in response to an activation protocol, right panel (600 ms depolarizations from 10 to +100 mV in variable steps, 10 mV and then 5 mV after 70 mV, from a holding potential of −90 mV; sweep-to-sweep interval = 5 s). (d) Normalized current–voltage curve from (c). Reversal potential can be obtained by linear regression, as indicated. The averaged value obtained by this method ($n$ = 5) gives $E_{rev}$ = −52.1 ± 10.3 mV, which corresponds to $P_{Ca}/P_{Na}$ = 0.07 ± 0.02 ($n$ = 5) when corrected for the liquid junction potential (−17 mV).

interactions with the proposed S4–S5 linker closed state pose [26].

Our studies demonstrate that destabilizing the helical structure of the neck causes negative shifts in $V_{1/2,act}$. The largest perturbation, 7Gly in which two full helical turns of the neck are glycines, has effects that are of the same magnitude as activation gate disruption (Table 1). In both cases, there are parallel shifts in $V_{1/2,inact}$ indicating that activation and inactivation are tightly coupled. Previous work with $Na_VSulP$ showed that coiled-coil disruption slowed inactivation kinetics by more than an order of magnitude, suggesting this structure as a role in accelerating inactivation [29]. Unlike these effects, which were caused by disruption further from the pore, destabilization of the $Na_VSp1$ neck had minimal impact on inactivation time constants (Fig. S7f and g). Moreover, examination of a coiled-coil mutation, R242E, equivalent to one from $Na_VSulP$ that caused a dramatic slowing of inactivation, negatively shifted $V_{1/2,act}$ but failed to produce a similar effect on $Na_VSp1$ inactivation kinetics (Fig. S8d). Thus, the major role of the neck is to stabilize the channel closed state.

Our studies lead us to propose the following model for $BacNa_V$ gating (Fig. 7). In the closed state, represented by the $Na_VAe1p$ structure (Fig. 1), the intracellular side of the channel central pore is occluded by the activation gate residue constriction ($Na_VAe1p$ M241). Opening would proceed with a radial expansion of this region [15] accompanied by an order → disorder transition in the neck. The neck region is a site of potential disorder [28]. The abundance of polar and charged neck residues (Fig. 2g) may aid the transition to this state and assist in permeant ion escape into the cytoplasm (Fig. 7). Whether such a state resembles the proposed $BacNa_V$ open state model [20] is unclear, as much of the end of S6, including the activation gate equivalent of $Na_VAe1p$ Met241, is absent from the $Na_VMs$ structure. Eukaryotic $Na_V$s and $Ca_V$s lack an equivalent of the C-terminal tail; however, the prevalence of similarly located C-terminal coiled-coil domains among diverse eukaryotic VGICs [41–43] and the importance of the intervening region that connects S6 to the coiled coils for channel regulation by a diverse factors [54,55] suggests that the essence of this proposed $BacNa_V$ mechanism has parallels in eukaryotic VGICs.

The ionic radii and coordination geometries of sodium and calcium ions are similar [2]. Hence, the $Na_VAe1p$ outer ion position, revealed by calcium, appears to mark the site of entry and partial dehydration as the permeant ion interacts with the (+1) residues and passes into the selectivity filter. This role in ion coordination agrees with the observation that a single S → D change at the NaChBac ($Na_VBh1$) (+1) position alters selectivity for calcium over sodium by ~200-fold [48] and with simulations suggesting that residues forming the outer ion site may be involved in ion recruitment [35]. The outer ion site may also participate in the divalent ion block described for NaChBac ($Na_VBh1$) [11,17] and the NaChBac/$Na_VRh$ selectivity filter chimera [17] as it corresponds well with the predicted “site 1” blocking site from molecular dynamics simulations [35]. It is also striking that structural changes at the (+1) serine cause substantial alterations to the size of the selectivity filter entrance in the putative inactivated conformation of $Na_VAb$ [16] and in $Na_VRh$, where the (+1) serine occludes the pore (Fig. S4). Thus, this outer ion site not only may be important for engagement of permeant and blocking ions but also may participate in rearrangements leading to slow inactivation [56].

Observation of an outer ion binding site in the selectivity filter together with the prior discovery of a selectivity filter inner ion site [17] (Fig. 3c) and

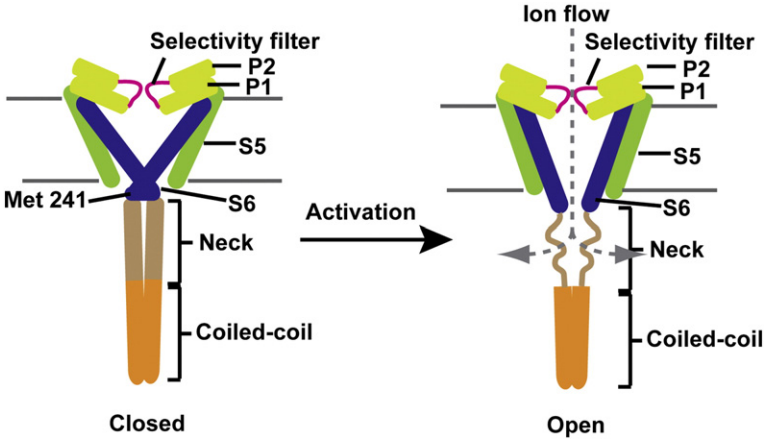


**Fig. 7.** Cartoon model of $BacNa_V$ gating. Activation of $BacNa_V$s is proposed to involve the expansion of the pore at the activation gate (Met241) and an order → disorder transition in the neck region. Ions can escape into the cytoplasm through spaces created by the neck region. Channel elements are colored as in Fig. 1. VSDs are not shown.

strong sequence and structural conservation of this region (Figs. 1c and 3c) shows that BacNa$_V$ selectivity filters possess more than one ion binding site. It seems possible, especially given the ~10-Å separation between outer and inner ion sites, that multiple ions may occupy the selectivity filter simultaneously. This situation would be tantalizingly close to accepted ideas regarding multi-ion pores in mammalian Na$_V$ and Ca$_V$ counterparts [2,31,32,34], not unlike that of potassium channels [57], in line with recent computational studies of BacNa$_V$ filters [58], and argues against the single ion pore model suggested in the initial BacNa$_V$ structure analysis [15].

Identification of the outer ion binding site uncovered a previously unknown role for the analogous conserved (+1) position in mammalian Ca$_V$s as an important determinant for calcium selectivity. Notably, despite its more exposed location, the impact of neutralization of the (+1) position is equivalent to that of neutralization of the (0) position glutamate that resides deeper in the selectivity filter (Fig. 4d), strongly suggesting that it may interact directly with the permeant ion. These results demonstrate a deep commonality between BacNa$_V$s and eukaryotic voltage-gated channels that should facilitate understanding ion permeation and gating in the superfamily.

## Materials and Methods

### Crystallization

Na$_V$Ae1p was expressed and purified in β-dodecyl maltoside (DDM) as previously described [19]. For high-calcium-condition crystals, purified protein was concentrated to 15 mg ml$^{-1}$ by centrifugal filtration (Amicon® Ultra-15 100-kDa molecular mass cutoff; Millipore) and mixed with 5 M trimethylamine oxide (TMAO [59,60]) creating a solution of 13.5 mg ml$^{-1}$ protein, 0.25 mM DDM, 0.5 M TMAO, 200 mM NaCl, and 20 mM Na–Hepes (pH 8.0). The protein was crystallized using hanging-drop vapor diffusion at 4 °C over a reservoir of 200 mM $CaCl_2$, 30% polyethylene glycol (PEG) 400, and 100 mM Na-acetate (pH 5.0). We laid 0.7 μl of protein–TMAO solution on a 0.7-μl drop of mother liquor that had been mixed with agarose to a final concentration of 0.25% and left to solidify at room temperature for 1 min. *I*222 crystals grew from precipitate to a final size of ~200 μm × 70 μm × 15 μm after 3 weeks.

For low-calcium-condition crystals, protein was concentrated to 13.5 mg ml$^{-1}$ (Amicon® Ultra-15 100-kDa molecular weight cutoff; Millipore) following exchange into 0.25 mM DDM, 200 mM NaCl, and 20 mM Na–Hepes (pH 8.0), during the last size-exclusion chromatography purification step. *P*4$_2$ crystals were grown by hanging-drop vapor diffusion at 4 °C from equal volumes of protein reservoir solution of 200 mM $MgCl_2$, 30% PEG 400, and 100 mM 4-morpholineethanesulfonic acid (pH 6.5). Crystals appeared in 2 days and grew to ~200 μm × 50 μm × 50 μm in ~2 weeks.

Na$_V$Ae1p H245G was expressed and was purified as Na$_V$Ae1p [19] using a final size-exclusion chromatography buffer of 0.3 mM DDM, 200 mM NaCl, 2 mM $MgCl_2$, and 20 mM Na–Hepes (pH 8.0). Purified protein was concentrated to 13.5 mg ml$^{-1}$ (Amicon® Ultra-15 100-kDa molecular weight cutoff; Millipore). We set up 1-μl hanging drops at 4 °C using a 24-well VDX Plate™ (Hampton Research) over a reservoir of 28% PEG 400 and 100 mM Na-acetate (pH 4.5). *I*222 crystals grew overnight and reached maximal proportions of ~300 μm × 75 μm × 15 μm after 2 weeks.

### Data collection, structure determination, and refinement

Crystals were frozen directly into liquid $N_2$ for data collection. Diffraction data were collected at Advanced Light Source Beamline 8.3.1, Lawrence Berkeley National Laboratory, integrated with MOSFLM 7.0.4 [61] and scaled with SCALA (3.3.20) [62]. Phase information was obtained by molecular replacement with an ensemble model based on the 3RVY, 4DXW, and 4EKW PDs using Phaser (2.1.4) [63]. Model was improved using cycles of manual rebuilding, Coot (0.7) [64], and refinement, Refmac (5.7.32) [65]. NCS-averaged maps improved apparent electron density and allowed placing of most of the side chains. For the high-calcium structure, initial tight NCS restraints were employed and later relaxed for all segments except for residues 183–208 and 214–220. For both the low-calcium structure and the Na$_V$Ae1p H245G mutant, tight NCS restraints were employed throughout.

### Two-electrode voltage-clamp electrophysiology

Human Ca$_V$1.2 (α$_1$C77; GenBank CAA84346), rat Ca$_V$β$_{2a}$ (GenBank NP 446303), and Ca$_V$α$_2$δ-1 (GenBank NM_00182276) were used for two-electrode voltage clamp experiments in *Xenopus* oocytes. Mutations were introduced using QuikChange (Stratagene, La Jolla, CA, USA). Linearized cDNA was translated into capped mRNA using the T7 mMessenger kit (Ambion). We injected 50 nl of Ca$_V$1.2α$_1$, Ca$_V$β$_{2a}$, and Ca$_V$α$_2$δ-1 mRNA at a 1:1:1 molar ratio into *Xenopus* oocytes. Two-electrode voltage-clamp experiments were performed 2–3 days post-injection. Oocytes were injected with 50 nl of 100 mM BAPTA 4′ before recording to minimize calcium-activated chloride currents. Recording solutions contained 100 mM LiOH, $Ca(NO_3)_2$ at the concentration indicated, and 10 mM Hepes, adjusted to pH 7.4 using $HNO_3$. $Ca^{2+}$ concentrations were verified using a $Ca^{2+}$ electrode. The solution with a nominal free $Ca^{2+}$ concentration of 3 nM contained 170 μM $Ca(NO_3)_2$ and 15 mM ethylene glycol-bis( 2-aminoethylether)-N, N,N′,N′-tetraacetic acid (EGTA). Buffered solutions with nominal free $Ca^{2+}$ concentrations of 100 nM, 300 nM, and 1 μM were also tested and gave results similar to the corresponding solutions in which $Ca^{2+}$ was not buffered by EGTA. Electrodes were filled with 3 M KCl and had resistances of 0.3–1.0 MΩ. Recordings were conducted at room temperature from a holding potential of −90 mV. Leak currents were subtracted using a P/4 protocol. Currents were analyzed with Clampfit 8.2 (Axon Instruments). All results are from at least two independent oocyte batches. Dose–response curves were calculated as follows: $I_x/I_{3nMCa} = 1/(1 + x/IC_{50})$, where $I_x$ is the current at the $Ca^{2+}$ concentration $x$ and $IC_{50}$ is the half-maximal inhibitory concentration.

### Patch-clamp electrophysiology

BacNa$_V$s from *S. pomeroyi* (NavSp1) and *A. ehrlichei* (Na$_V$Ae1) were cloned into the pIRES2-EGFP vector (Clontech, Mountain View, CA, USA). All the Na$_V$Sp1 mutants were made using the QuikChange® Site-Directed Mutagenesis Kit (Stratagene) and sequenced before recordings. Human embryonic kidney cells (HEK 293) were grown at 37 °C under 5% $CO_2$, in a Dulbecco's modified Eagle's medium supplemented with 10% fetal bovine serum, 10% L-glutamine, and antibiotics (100 IU ml$^{-1}$ penicillin and 100 mg ml$^{-1}$ streptomycin) (University of California, San Francisco Cell Culture Facility). HEK 293 cells were transfected (in 35-mm-diameter wells) with LipofectAMINE™ 2000 (Invitrogen, Carlsbad, CA, USA) and plated onto coverslips coated with Matrigel (BD Biosciences, San Diego, CA, USA). We used 2 μg of DNA except for the L212A and I216A for which 4 μg of DNA was used to increase current amplitude.

Transfected cells were identified visually enhanced green fluorescent protein (EGFP) expression. Whole cell patch-clamp [66] was used to record $Na^+$ current at room temperature (23 ± 2 °C) 48–72 h post-transfection. Acquisition and analysis were performed using pCLAMP 9 (Molecular Devices, Sunnyvale, CA, USA) and an Axopatch 200B amplifier (Molecular Devices). Pipettes were pulled from borosilicate glass capillaries (TW150F-3; World Precision Instruments, Sarasota, FL, USA) and polished (MF-900 microforge; Narishige, Tokyo, Japan) to obtain 2–3 MΩ resistances. Sixty to eighty percent of the voltage error due to the series resistance was compensated. Unless stated otherwise, pipette solution contained the following, in millimolars: 120, Cs methane sulfonate; 8, NaCl; 10, EGTA; 2, Mg-ATP; and 20, Hepes (pH 7.4 with CsOH). Bath solution contained the following, in millimolars: 155, NaCl; 1, $CaCl_2$; 1, $MgCl_2$; 5, KCl; 10, Hepes; and 10, glucose (pH 7.4 with NaOH).

For reversal potential measurements determining the $Na^+$ and $Ca^{2+}$ relative permeabilities, pipette solution contained the following, in millimolars: 100, Na-Gluconate; 10, NaCl; 10, EGTA; and 20, Hepes (pH 7.4 adjusted with NaOH; total [Na] is 130). For tail protocol experiments on Na$_V$Sp1 3Gly, the pipette solution contained the following, in millimolars: 30, Na-Gluconate; 10, NaCl; 10, EGTA; 20, Hepes; and 70, NMDG-Cl (pH 7.4 adjusted with NaOH; total [Na] is 45). External solution in both was as follows, in millimolars: 5, NMDG-Cl; 100, $CaCl_2$; and 20, Hepes (pH 7.4 adjusted with CaOH; total [Ca] is 107.5). The permeability ratio of $Ca^{2+}$ over $Na^+$ was estimated using the following equation:

$$P_{Ca}/P_{Na} = a_{Na,int}[\exp(E_{rev}F/RT)]\,[\exp(E_{rev}F/RT)+1] / (4a_{Ca,ext}),$$

where $R$, $T$, $F$, and $E_{rev}$ are the gas constant, absolute temperature, Faraday constant, and reversal potential, respectively (int, internal; ext, external) [2]. $Ca^{2+}$ and $Na^+$ activity coefficients were estimated as follows:

$$a_s = g_s[X_s],$$

where activity, $a_s$, is the effective concentration of an ion in solution, s, related to the nominal concentration $[X_s]$ by the activity coefficient $\gamma_s$. $\gamma_s$ was calculated from the Davies equation. The calculated activity coefficients were $\gamma_{(Na)int} = 0.76$ and $\gamma_{(Ca)ext} = 0.33$. The liquid junction potentials were calculated by the JPCalc program (P. Barry) within Clampex (Molecular Devices) and taken into account to determine $E_{rev}$.

### Accession codes

Crystallographic coordinates and structure factors are deposited with the PDB will be released immediately upon publication: 4LTO, Na$_V$Ae1p, crystal I, high calcium; 4LTP, Na$_V$Ae1p, crystal II, high calcium; 4LTQ, Na$_V$Ae1p, low calcium; 4LTR, Na$_V$Ae1p H245G, low calcium.

## Acknowledgements

We thank Christine Rumpf and Ahmed Rohaim for expert molecular biology assistance and J. Holton and G. Meigs at Advanced Light Source Beamline 8.3.1 for data collection assistance. We thank K. Brejc, L. Jan, and E. Reuveny for helpful manuscript comments and Minor laboratory members for support throughout these studies. This work was supported by National Institutes of Health grants R01-HL080050, R01-DC007664, and U54-GM094625 and the American Heart Association grant 0740019N to D.L.M.; an American Heart Association Postdoctoral Fellowship to D.S.; and Fulbright Scholarship and a Monahan Foundation Fellowship to F.A.-A. G.L. was supported by a Marie Curie International Outgoing Fellowship within the 7th European Community Framework Programme. D.L.M. is an American Heart Association Established Investigator.

**Author Contributions**: D.S., F.F., and D.L.M. conceived the study and designed the experiments. D.S., F.F., F.A.-A., S.W., and S.R. performed the experiments. D.S., S.W., and S.R. purified the proteins. D.S. grew the crystals and collected diffraction data. D.S. and F.F. solved and refined the structures and analyzed the data. F.F., F.A.-A., and C.A. designed and performed electrophysiological experiments and analyzed the data. G.L. and D.L.M. supervised the electrophysiology and analyzed data. D.L.M. analyzed data and provided guidance and support throughout. D.S., F.F., F.A.-A., C.A., G.L., and D.L.M. wrote the paper.

**Conflict of Interest**: The authors declare that there are no competing interests.

## Appendix A. Supplementary data

Supplementary data to this article can be found online at http://dx.doi.org/10.1016/j.jmb.2013.10.010.

*Received 24 July 2013;*
*Received in revised form 20 September 2013;*
*Accepted 5 October 2013*
Available online 10 October 2013

***Keywords:***
voltage-gated sodium channel;
X-ray crystallography;
electrophysiology;
ion binding;
voltage-gated calcium channel

This is an open-access article distributed under the terms of the Creative Commons Attribution-NonCommercial-ShareAlike License, which permits non-commercial use, distribution, and reproduction in any medium, provided the original author and source are credited.

† D.S. and F.F. contributed equally to this work.

***Abbreviations used:***
VGIC, voltage-gated ion channel; VSD, voltage-sensing domain; PD, pore domain; DDM, β-dodecyl maltoside; PEG, polyethylene glycol; EGTA, ethylene glycol-bis( 2-aminoethylether)-N, N,N′,N′-tetraacetic acid.

## References

[1] Catterall WA. From ionic currents to molecular mechanisms: the structure and function of voltage-gated sodium channels. Neuron 2000;26:13–25.
[2] Hille B. Ion channels of excitable membranes. 3rd ed. Sunderland, MA: Sinauer Associates, Inc.; 2001.
[3] Mantegazza M, Curia G, Biagini G, Ragsdale DS, Avoli M. Voltage-gated sodium channels as therapeutic targets in epilepsy and other neurological disorders. Lancet Neurol 2010;9:413–24.
[4] Bhattacharya A, Wickenden AD, Chaplan SR. Sodium channel blockers for the treatment of neuropathic pain. Neurotherapeutics 2009;6:663–78.
[5] Etheridge SM. Paralytic shellfish poisoning: seafood safety and human health perspectives. Toxicon 2010;56:108–22.
[6] Yu FH, Catterall WA. The VGL-chanome: a protein superfamily specialized for electrical signaling and ionic homeostasis. Sci STKE 2004;2004:re15.
[7] Yu FH, Yarov-Yarovoy V, Gutman GA, Catterall WA. Overview of molecular relationships in the voltage-gated ion channel superfamily. Pharmacol Rev 2005;57:387–95.
[8] Heinemann SH, Terlau H, Stuhmer W, Imoto K, Numa S. Calcium channel characteristics conferred on the sodium channel by single mutations. Nature 1992;356:441–3.
[9] Favre I, Moczydlowski E, Schild L. On the structural basis for ionic selectivity among $Na^+$, $K^+$, and $Ca^{2+}$ in the voltage-gated sodium channel. Biophys J 1996;71:3110–25.
[10] Tang S, Mikala G, Bahinski A, Yatani A, Varadi G, Schwartz A. Molecular localization of ion selectivity sites within the pore of a human L-type cardiac calcium channel. J Biol Chem 1993;268:13026–9.
[11] Ren D, Navarro B, Xu H, Yue L, Shi Q, Clapham DE. A prokaryotic voltage-gated sodium channel. Science 2001;294:2372–5.
[12] Koishi R, Xu H, Ren D, Navarro B, Spiller BW, Shi Q, et al. A superfamily of voltage-gated sodium channels in bacteria. J Biol Chem 2004;279:9532–8.
[13] Irie K, Kitagawa K, Nagura H, Imai T, Shimomura T, Fujiyoshi Y. Comparative study of the gating motif and C-type inactivation in prokaryotic voltage-gated sodium channels. J Biol Chem 2010;285:3685–94.
[14] Charalambous K, Wallace BA. NaChBac: the long lost sodium channel ancestor. Biochemistry 2011;50:6742–52.
[15] Payandeh J, Scheuer T, Zheng N, Catterall WA. The crystal structure of a voltage-gated sodium channel. Nature 2011;475:353–8.
[16] Payandeh J, Gamal El-Din TM, Scheuer T, Zheng N, Catterall WA. Crystal structure of a voltage-gated sodium channel in two potentially inactivated states. Nature 2012;486:135–9.
[17] Zhang X, Ren W, DeCaen P, Yan C, Tao X, Tang L, et al. Crystal structure of an orthologue of the NaChBac voltage-gated sodium channel. Nature 2012;486:130–4.
[18] McCusker EC, D'Avanzo N, Nichols CG, Wallace BA. A simplified bacterial "Pore" provides insight into the assembly, stability and structure of sodium channels. J Biol Chem 2011;286:16386–91.
[19] Shaya D, Kreir M, Robbins RA, Wong S, Hammon J, Bruggemann A, et al. Voltage-gated sodium channel (NaV) protein dissection creates a set of functional pore-only proteins. Proc Natl Acad Sci U S A 2011;108:12313–8.
[20] McCusker EC, Bagneris C, Naylor CE, Cole AR, D'Avanzo N, Nichols CG, et al. Structure of a bacterial voltage-gated sodium channel pore reveals mechanisms of opening and closing. Nat Commun 2012;3:1102.
[21] Caprini M, Ferroni S, Planells-Cases R, Rueda J, Rapisarda C, Ferrer-Montiel A, et al. Structural compatibility between the putative voltage sensor of voltage-gated $K^+$ channels and the prokaryotic KcsA channel. J Biol Chem 2001;276:21070–6.
[22] Lu Z, Klem AM, Ramu Y. Ion conduction pore is conserved among potassium channels. Nature 2001;413:809–13.
[23] Lu Z, Klem AM, Ramu Y. Coupling between voltage sensors and activation gate in voltage-gated $K^+$ channels. J Gen Physiol 2002;120:663–76.
[24] Arrigoni C, Schroeder I, Romani G, Van Etten JL, Thiel G, Moroni A. The voltage-sensing domain of a phosphatase gates the pore of a potassium channel. J Gen Physiol 2013;141:389–95.
[25] Long SB, Campbell EB, Mackinnon R. Crystal structure of a mammalian voltage-dependent Shaker family $K^+$ channel. Science 2005;309:897–903.
[26] Long SB, Tao X, Campbell EB, MacKinnon R. Atomic structure of a voltage-dependent $K^+$ channel in a lipid membrane-like environment. Nature 2007;450:376–82.
[27] Jiang Y, Lee A, Chen J, Ruta V, Cadene M, Chait BT, et al. X-ray structure of a voltage-dependent $K^+$ channel. Nature 2003;423:33–41.
[28] Powl AM, O'Reilly AO, Miles AJ, Wallace BA. Synchrotron radiation circular dichroism spectroscopy-defined structure of the C-terminal domain of NaChBac and its role in channel assembly. Proc Natl Acad Sci U S A 2010;107:14064–9.
[29] Irie K, Shimomura T, Fujiyoshi Y. The C-terminal helical bundle of the tetrameric prokaryotic sodium channel accelerates the inactivation rate. Nat Commun 2012;3:793.
[30] Mio K, Mio M, Arisaka F, Sato M, Sato C. The C-terminal coiled-coil of the bacterial voltage-gated sodium channel NaChBac is not essential for tetramer formation, but stabilizes subunit-to-subunit interactions. Prog Biophys Mol Biol 2010;103:111–21.

[31] Begenisich T. Molecular properties of ion permeation through sodium channels. Annu Rev Biophys Biophys Chem 1987;16:247–63.
[32] Tsien RW, Hess P, McCleskey EW, Rosenberg RL. Calcium channels: mechanisms of selectivity, permeation, and block. Annu Rev Biophys Biophys Chem 1987;16:265–90.
[33] Yang J, Ellinor PT, Sather WA, Zhang JF, Tsien RW. Molecular determinants of $Ca^{2+}$ selectivity and ion permeation in L-type $Ca^{2+}$ channels. Nature 1993;366:158–61.
[34] Hess P, Tsien RW. Mechanism of ion permeation through calcium channels. Nature 1984;309:453–6.
[35] Zhang X, Xia M, Li Y, Liu H, Jiang X, Ren W, et al. Analysis of the selectivity filter of the voltage-gated sodium channel Na(v)Rh. Cell Res 2012;23:409–22.
[36] Carnevale V, Treptow W, Klein ML. Sodium ion binding sites and hydration in the lumen of a bacterial ion channel from molecular dynamics simulations. J Phys Chem Lett 2011;2:2504–8.
[37] Karplus PA, Diederichs K. Linking crystallographic model and data quality. Science 2012;336:1030–3.
[38] Evans PR, Murshudov GN. How good are my data and what is the resolution? Acta Crystallogr Sect D Biol Crystallogr 2013;69:1204–14.
[39] Diederichs K, Karplus PA. Better models by discarding data? Acta Crystallogr Sect D Biol Crystallogr 2013;69:1215–22.
[40] Uysal S, Vasquez V, Tereshko V, Esaki K, Fellouse FA, Sidhu SS, et al. Crystal structure of full-length KcsA in its closed conformation. Proc Natl Acad Sci U S A 2009;106:6644–9.
[41] Howard RJ, Clark KA, Holton JM, Minor DL. Structural insight into KCNQ (Kv7) channel assembly and channelopathy. Neuron 2007;53:663–75.
[42] Wiener R, Haitin Y, Shamgar L, Fernandez-Alonso MC, Martos A, Chomsky-Hecht O, et al. The KCNQ1 (Kv7.1) COOH terminus, a multitiered scaffold for subunit assembly and protein interaction. J Biol Chem 2008;283:5815–30.
[43] Tsuruda PR, Julius D, Minor DL. Coiled coils direct assembly of a cold-activated TRP channel. Neuron 2006;51:201–12.
[44] Chovancova E, Pavelka A, Benes P, Strnad O, Brezovsky J, Kozlikova B, et al. CAVER 3.0: a tool for the analysis of transport pathways in dynamic protein structures. PLoS Comput Biol 2012;8:e1002708.
[45] Lomize MA, Lomize AL, Pogozheva ID, Mosberg HI. OPM: orientations of proteins in membranes database. Bioinformatics 2006;22:623–5.
[46] Pidcock E, Moore GR. Structural characteristics of protein binding sites for calcium and lanthanide ions. J Biol Inorg Chem 2001;6:479–89.
[47] Zheng H, Chruszcz M, Lasota P, Lebioda L, Minor W. Data mining of metal ion environments present in protein structures. J Inorg Biochem 2008;102:1765–76.
[48] Yue L, Navarro B, Ren D, Ramos A, Clapham DE. The cation selectivity filter of the bacterial sodium channel, NaChBac. J Gen Physiol 2002;120:845–53.
[49] Parent L, Gopalakrishnan M. Glutamate substitution in repeat IV alters divalent and monovalent cation permeation in the heart $Ca^{2+}$ channel. Biophys J 1995;69:1801–13.
[50] Findeisen F, Minor DL. Disruption of the IS6-AID linker affects voltage-gated calcium channel inactivation and facilitation. J Gen Physiol 2009;133:327–43.
[51] Bagriantsev SN, Clark KA, Minor DL. Metabolic and thermal stimuli control K(2P)2.1 (TREK-1) through modular sensory and gating domains. EMBO J 2012;31:3297–308.
[52] O'Neil KT, DeGrado WF. A thermodynamic scale for the helix-forming tendencies of the commonly occurring amino acids. Science 1990;250:646–51.
[53] Doyle DA, Morais Cabral J, Pfuetzner RA, Kuo A, Gulbis JM, Cohen SL, et al. The structure of the potassium channel: molecular basis of $K^+$ conduction and selectivity. Science 1998;280:69–77.
[54] Xu Q, Chang A, Tolia A, Minor DL. Structure of a Ca(2+)/CaM:Kv7.4 (KCNQ4) B-helix complex provides insight into M current modulation. J Mol Biol 2013;425:378–94.
[55] Haitin Y, Attali B. The C-terminus of Kv7 channels: a multifunctional module. J Physiol 2008;586:1803–10.
[56] Pavlov E, Bladen C, Winkfein R, Diao C, Dhaliwal P, French RJ. The pore, not cytoplasmic domains, underlies inactivation in a prokaryotic sodium channel. Biophys J 2005;89:232–42.
[57] Zhou Y, Morais-Cabral JH, Kaufman A, MacKinnon R. Chemistry of ion coordination and hydration revealed by a $K^+$ channel-Fab complex at 2.0 Å resolution. Nature 2001;414:43–8.
[58] Chakrabarti N, Ing C, Payandeh J, Zheng N, Catterall WA, Pomes R. Catalysis of $Na^+$ permeation in the bacterial sodium channel NaVAb. Proc Natl Acad Sci U S A 2013;110:11331–6.
[59] Jiang J, Lafer EM, Sousa R. Crystallization of a functionally intact Hsc70 chaperone. Acta Crystallogr Sect F Struct Biol Cryst Commun 2006;62:39–43.
[60] Clarke OB, Caputo AT, Hill AP, Vandenberg JI, Smith BJ, Gulbis JM. Domain reorientation and rotation of an intracellular assembly regulate conduction in Kir potassium channels. Cell 2010;141:1018–29.
[61] Leslie AGW. Recent changes to the MOSFLM package for processing film and image plate data. Joint CCP4 + ESF-EAMCB Newsletter of Protein Crystallography, 26; 1992.
[62] Evans PR. An introduction to data reduction: space-group determination, scaling and intensity statistics. Acta Crystallogr Sect D Biol Crystallogr 2011;67:282–92.
[63] McCoy AJ, Grosse-Kunstleve RW, Adams PD, Winn MD, Storoni LC, Read RJ. Phaser crystallographic software. J Appl Crystallogr 2007;40:658–74.
[64] Emsley P, Cowtan K. Coot: model-building tools for molecular graphics. Acta Crystallogr Sect D Biol Crystallogr 2004;60:2126–32.
[65] Collaborative Computational Project, Number 4. The CCP4 suite: programs for protein crystallography. Acta Crystallogr Sect D Biol Crystallogr 1994;50:760–3.
[66] Hamill OP, Marty A, Neher E, Sakmann B, Sigworth FJ. Improved patch-clamp techniques for high-resolution current recording from cells and cell-free membrane patches. Pflugers Arch 1981;391:85–100.

20 Sep 13

**Supplementary Material for:**

# Structure of a prokaryotic sodium channel pore reveals essential gating elements and an outer ion binding site common to eukaryotic channels

David Shaya[1*], Felix Findeisen[1*], Fayal Abderemane-Ali[5,6,7], Cristina Arrigoni[1], Stephanie Wong[1], Shailka Reddy Nurva[1], Gildas Loussouarn[5,6,7], and Daniel L. Minor, Jr.[1,2,3,4†]

[1]Cardiovascular Research Institute, [2]Departments of Biochemistry and Biophysics, and Cellular and Molecular Pharmacology, [3]California Institute for Quantitative Biomedical Research, University of California, San Francisco, California 94158-2330

[4]Physical Biosciences Science Division
Lawrence Berkeley National Laboratory
Berkeley, CA 94720 USA

[5]Institut National de la Santé et de la Recherche Médicale, UMR1087, Nantes, France
[6]Centre National de la Recherche Scientifique, UMR 6291, Nantes, France
[7]l'institut du thorax, L'UNAM, Université de Nantes, Nantes, France

* These authors contributed equally

[†]Correspondence: daniel.minor@ucsf.edu

**Inventory of Supplementary Material:**

Supplementary Figures S1-S10

Supplementary Tables S1-S3

Supplementary References

## Supplementary Figure S1

Shaya *et al.*

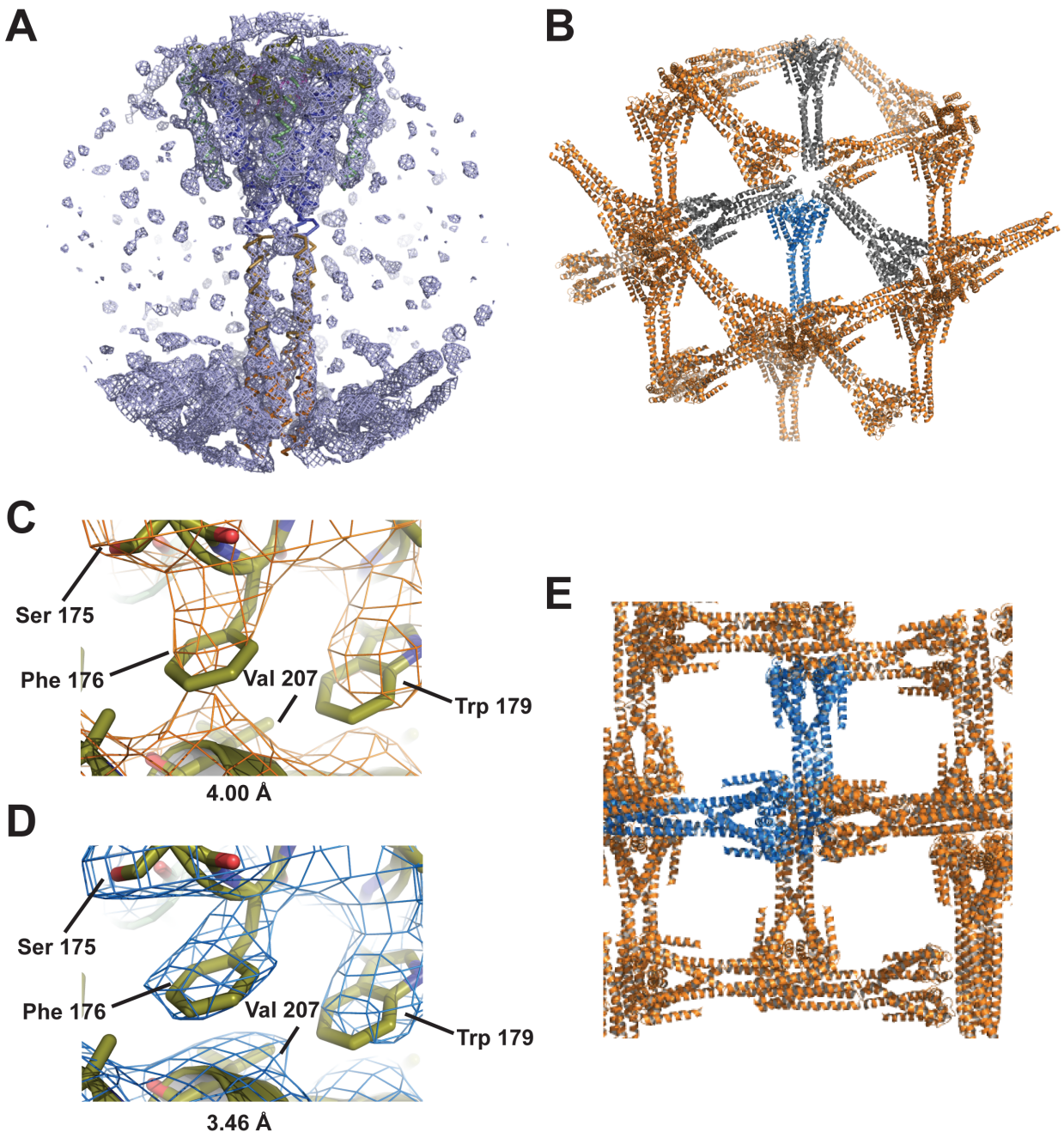


**Supplementary Figure S1 A,** Initial electron density map following molecular replacement using a model that only included the transmembrane domains. Map is contoured at 1.5σ. **B,** $Na_VAe1p$ I222 crystal packing. The asymmetric unit, a channel tetramer, is shown in marine. Three tetramers are shown in grey to aid in lattice visualization. Remaining molecules are shown in orange. **C, and D,** Representative 2Fo-Fc electron density contoured at 1σ for a portion of the electron density map including the P1 and P2 helices using data to **C,** 4.00Å and **D,** 3.46Å. **E,** $Na_VAe1p$ $P4_2$ crystal packing. The asymmetric unit, two channel tetramers, is shown in marine. Symmetry related molecules are shown in orange.

## Supplementary Figure S2

**Shaya *et al.***

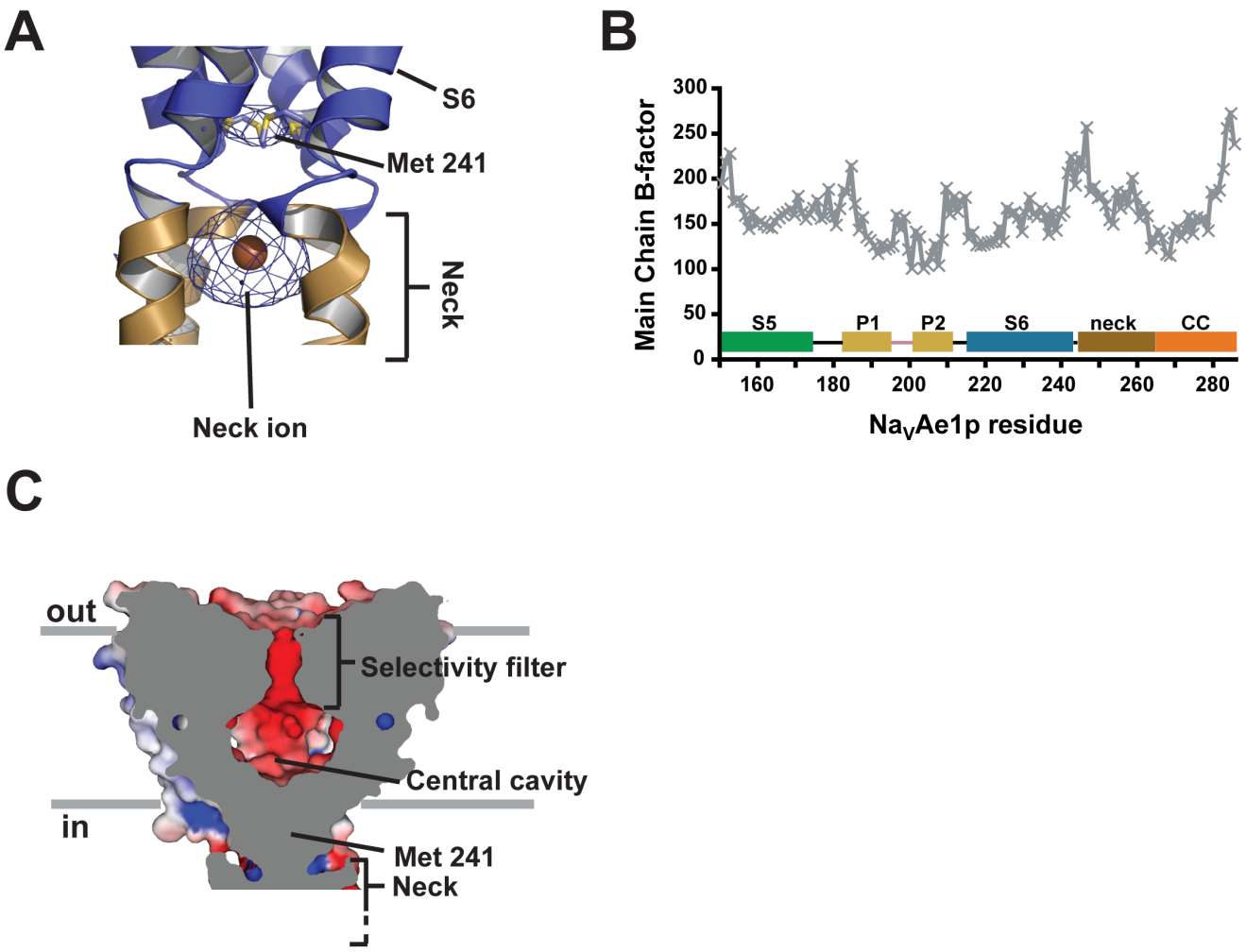


**Supplementary Figure S2 $Na_VAe1p$ structure details A,** $Na_VAe1p$ NCS-averaged anomalous difference map calculated at 6.5Å and contoured at 2.5σ. S6 and neck are colored blue and sand, respectively. Positions of Met241 and neck ion densities are indicated. Met241 sidechains are shown as sticks. **B,** Averaged $Na_VAe1p$ main chain B-factors. Secondary structure elements are indicated: S5 (green), S6 (blue), P1 and P2 (tan), neck (brown), and coiled-coil (orange). **C,** Electrostatic surface potential mapped on the $Na_VAe1p$ van der Waals surface, sliced open to show the central cavity and colored from -4 kT to +4 kT (red to blue). Grey lines indicate approximate lipid bilayer boundaries.

## Supplementary Figure S3



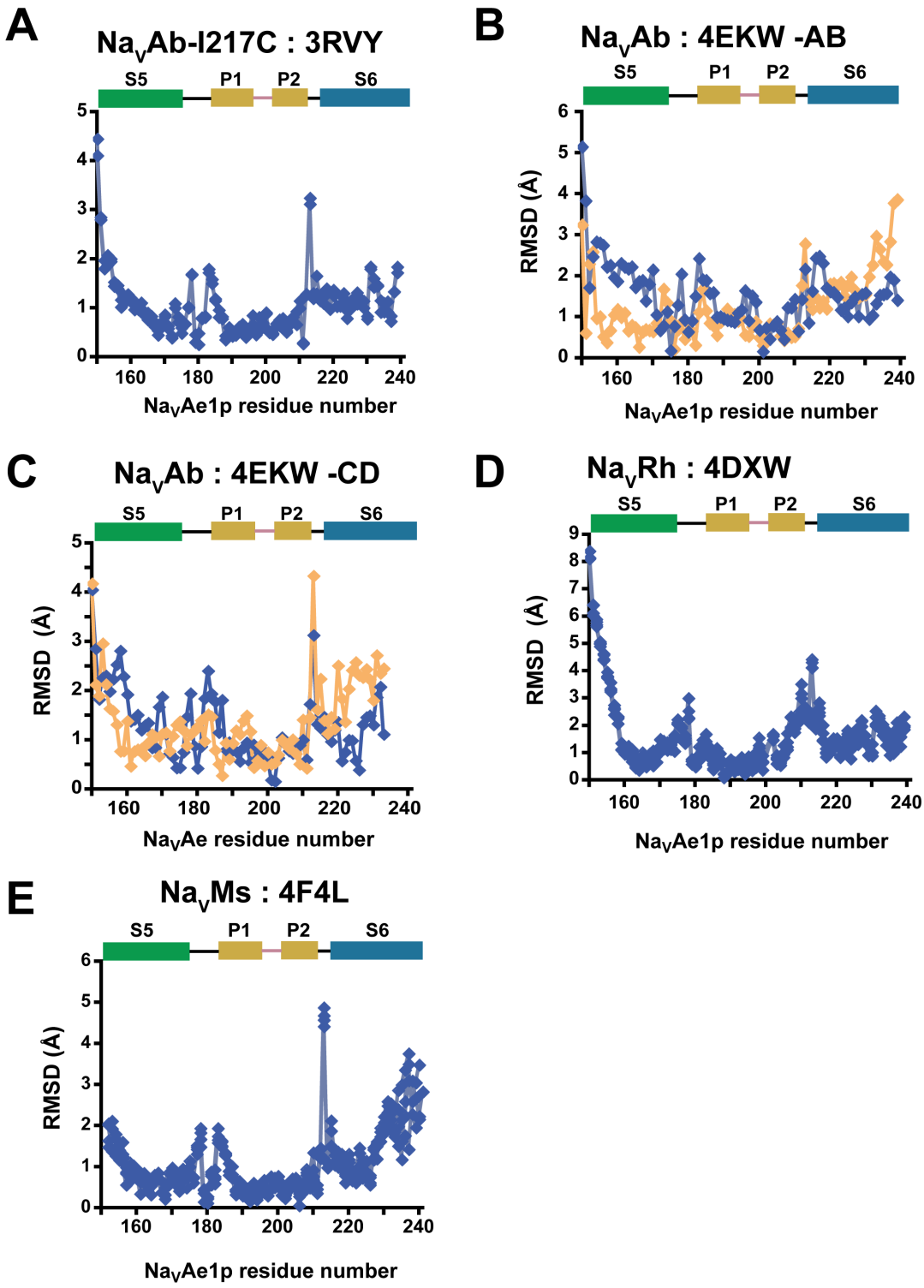


**Supplementary Figure S3 $Na_VAe1p$ and $BacNa_V$ pore domain comparisons** Residue by residue Cα RMSD plots comparing the $Na_VAe1p$ pore with the pore domains from: **A,** $Na_VAb$-I217C (3RVY)(Payandeh et al., 2011), **B,** $Na_VAb$, chains A (blue) and B (orange) (Payandeh et al., 2012), **C,** $Na_VAb$, chains C (blue) and D (orange) (Payandeh et al., 2012), **D,** $Na_VRh$ (Zhang et al., 2012), and **E**, $Na_VMs$ (McCusker et al., 2012). Secondary structure elements are indicated as S5 (green), S6 (blue), P1 and P2 (tan). Boundaries used in the superpositions are listed in Supplementary Table S3.

## Supplementary Figure S4



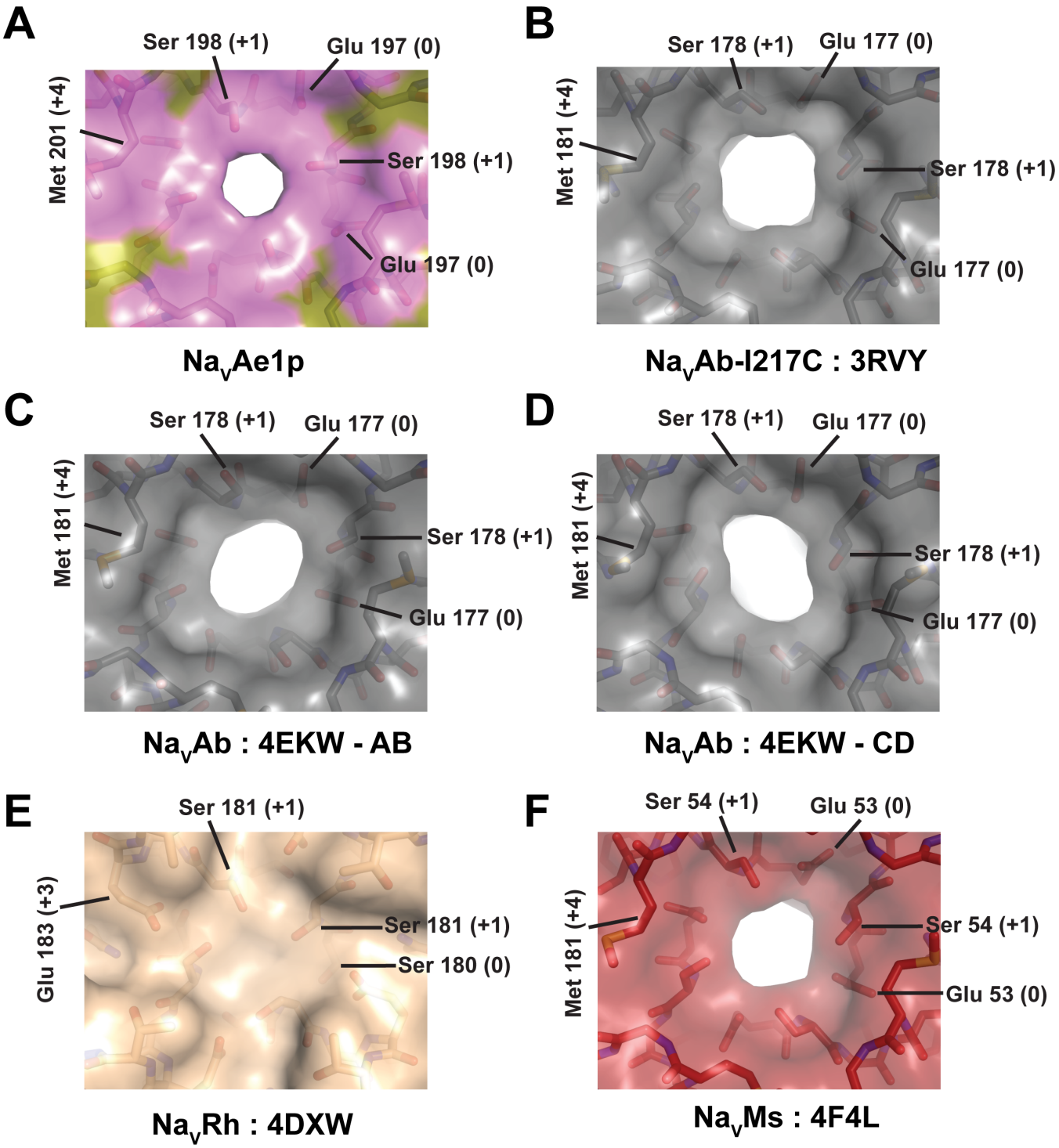


**Supplementary Figure S4** Semitransparent surfaces showing the selectivity filter extracellular side for: **A,** $Na_VAe1p$, **B,** $Na_VAb$ (Payandeh et al., 2011), **C,** $Na_VAb$ 'inactivated' conformation of chains A/B (Payandeh et al., 2012), **D,** $Na_VAb$ 'inactivated' conformation of chains C/D (Payandeh et al., 2012), **E,** $Na_VRh$ (Zhang et al., 2012), and **F,** $Na_VMs$ (McCusker et al., 2012). In all cases, select residues are labeled according to the scheme shown in Figure 4. $Na_VAe1p$ is colored violet (selectivity filter) and olive (P2 helix) as in Figure1. $Na_VAb$ is grey, $Na_VRh$ is wheat, and $Na_VMs$ is dark red.

# Supplementary Figure S5



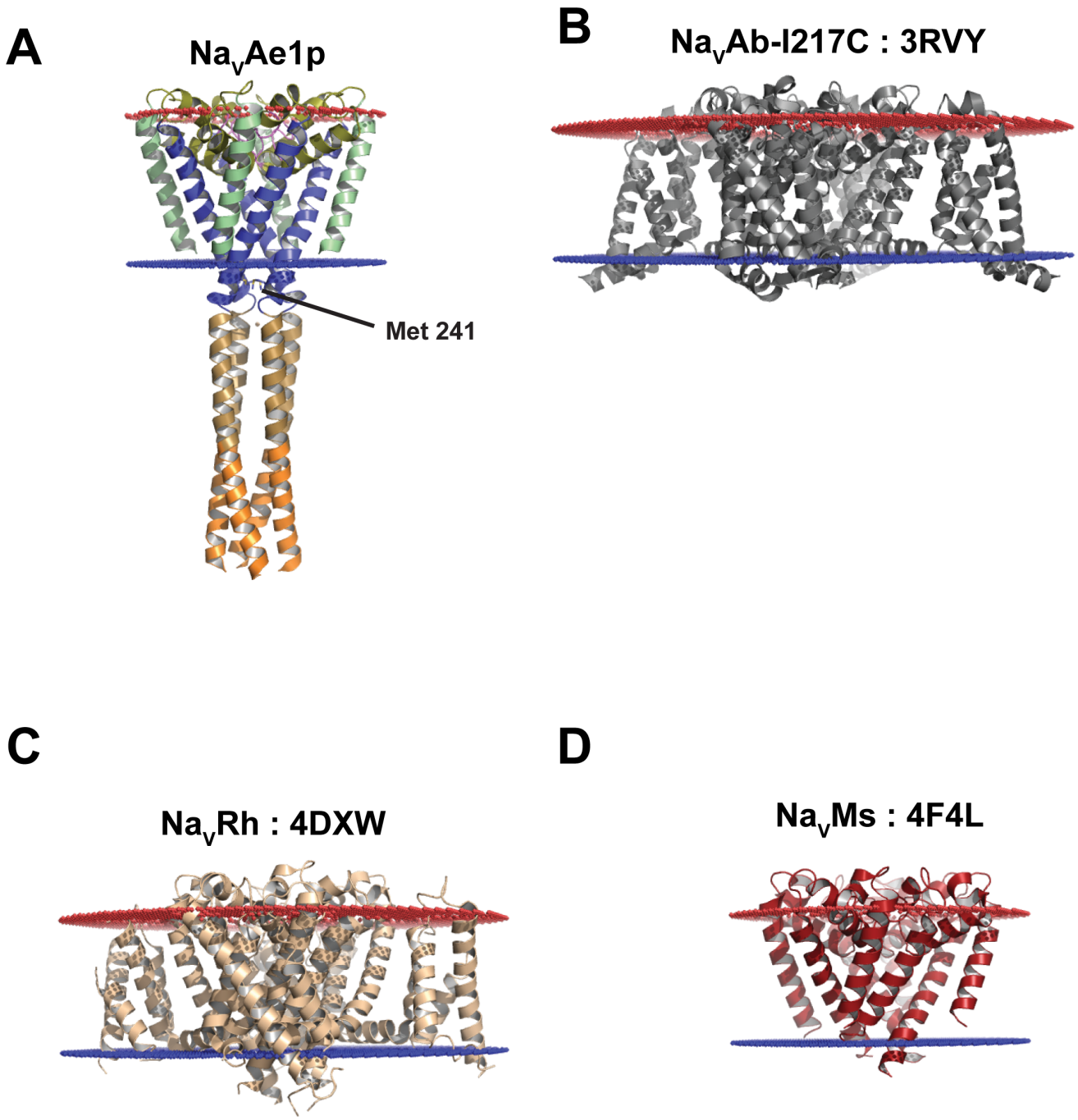


**Supplementary Figure S5** Predicted membrane hydrophobic layer boundaries. Transmembrane layers were calculated for: **A,** $Na_V$Ae1p, **B,** $Na_V$Ab I217C (3RVY)(Payandeh et al., 2011), **C,** $Na_V$Rh (4DXW)(Zhang et al., 2012), and **D,** $Na_V$Ms (4F4L)(McCusker et al., 2012), using the OPM server (http://opm.phar.umich.edu)(Lomize et al., 2006) and are represented by a red disk (boundary between hydrophobic layer and extracellular lipid head groups) and a blue disk (boundary between hydrophobic layer and intracellular lipid head groups).

## Supplementary Figure S6 Shaya *et al.*

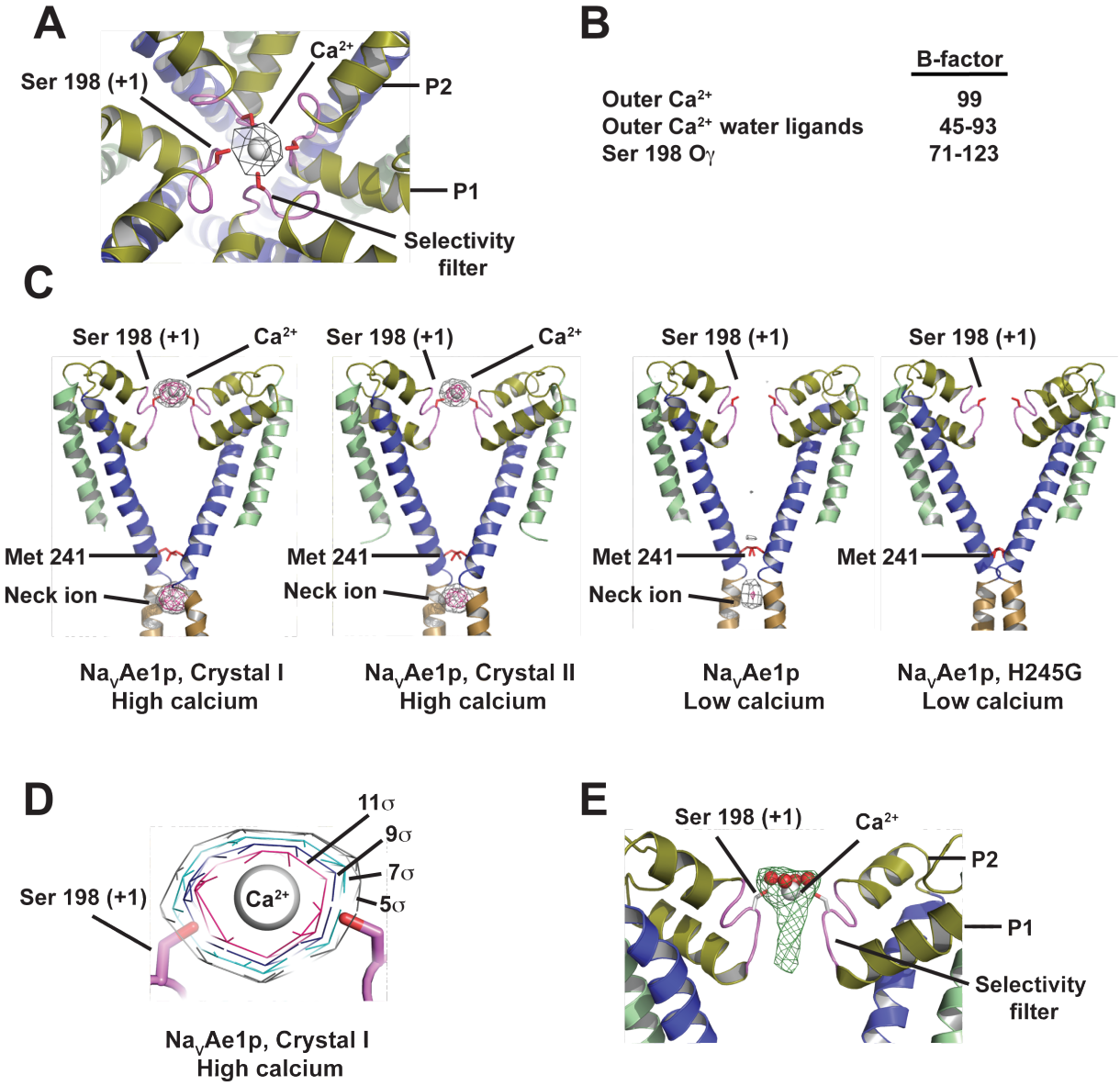


**Supplementary Figure S6 $Na_VAe1p$ difference maps A,** High calcium $Na_VAe1p$ anomalous difference map calculated at 6.5Å and contoured at 6.5σ showing a strong peak at the pore center close to the side chains of $Na_VAe1p$ Ser198. **B,** Temperature factors for outer ion and associated ligands. **C,** NCS-averaged anomalous difference maps calculated for the indicated datasets at 6.5Å. Contours show 5σ (grey) and 10σ (pink). The anomalous signal at the site for the pore metal is present in both high $Ca^{2+}$-structures but is absent in both low $Ca^{2+}$-structures. Anomalous signal at the neck ion site is present in all but the H245G structure. Select residues are indicated for orientation purposes. **D,** Closeup of the anomalous signal for the outer ion site in the $Na_VAe1p$, Crystal I, High calcium dataset. Contour levels are indicated. **E,** Fo-Fc map (green) of $Na_VAe1p$ selectivity filter region calculated using a protein model but lacking the outer ion and waters contoured at 3.0σ. Map shows electron density for the $Ca^{2+}$ ion and extends through the entire selectivity filter length. $Ca^{2+}$ is indicated as a white sphere, four water molecules are shown as red spheres. $Na_VAe1p$ is colored as in Figure 1.

## Supplementary Figure S7

**Shaya *et al.***

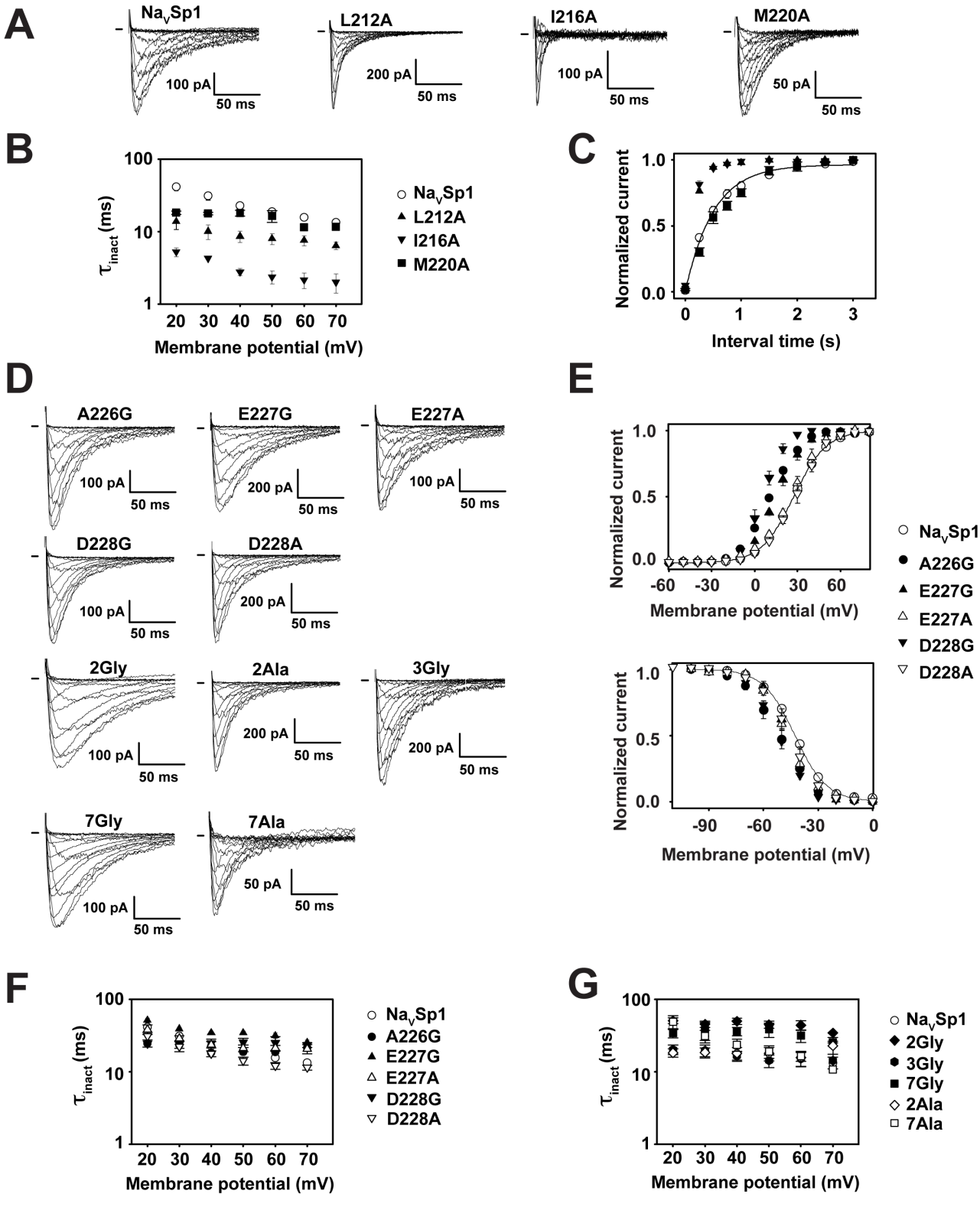

**Supplementary Figure S7 Functional studies of $Na_VSp1$, S6 mutants, and neck mutants** **A,** Representative $Na^+$ currents from $Na_VSp1$, L212A, I216A, and M220A in response to an activation protocol from -60 to +70 mV in 10 mV steps (cf. Figure 5B middle panel). **B,** Inactivation time constants for $Na_VSp1$, L212A, I216A, and M220A (n =3-8; error bars are ± s.e.m.). **C,** Recovery from inactivation for $Na_VSp1$, L212A, I216A, and M220A. Time interval between the pre-pulse (+30 mV, 300 ms) and the test-pulse (+30 mV, 300 ms) was varied from 0.25 to 3 s. The ratios between currents elicited by the two pulses were used to construct the recovery from inactivation curve. (n =3 to 7; ± s.e.m.). Recovery curve of $Na_VSp1$ is highlighted with a single exponential fit. **D,** Representative $Na^+$ currents from the indicated $Na_VSp1$ neck mutants in response to an activation protocol of -60 to +70 mV in 10 mV steps (cf. Figure 5B middle panel). **E,** Voltage dependences of activation (top) and inactivation (bottom) for $Na_VSp1$ and indicated mutants. **F and G,** Inactivation time constants for $Na_VSp1$ and indicated mutants (n = 4-8; error bars are ± s.e.m.).

# Supplementary Figure S8

**Shaya *et al.***

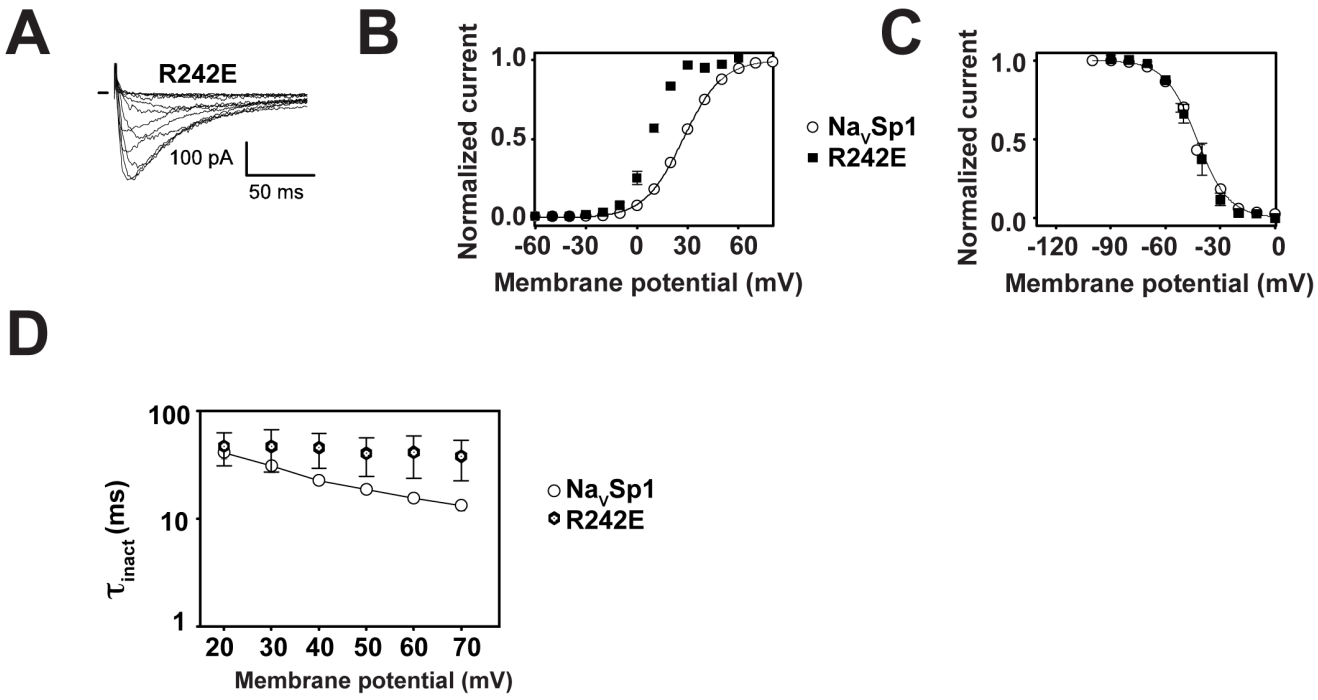


**Supplementary Figure S8 A,** Representative $Na^+$ currents from $Na_VSp1$ R242E in response to an activation protocol of -60 to +70 mV in 10 mV steps. **B,** Voltage dependence of activation and **C,** Voltage dependence of inactivation for $Na_VSp1$ and R242E. **D,** Inactivation time constants for NavSp1 and R242E (n =3-8; error bars are ±S.E.M).

# Supplementary Figure S9

Shaya *et al.*

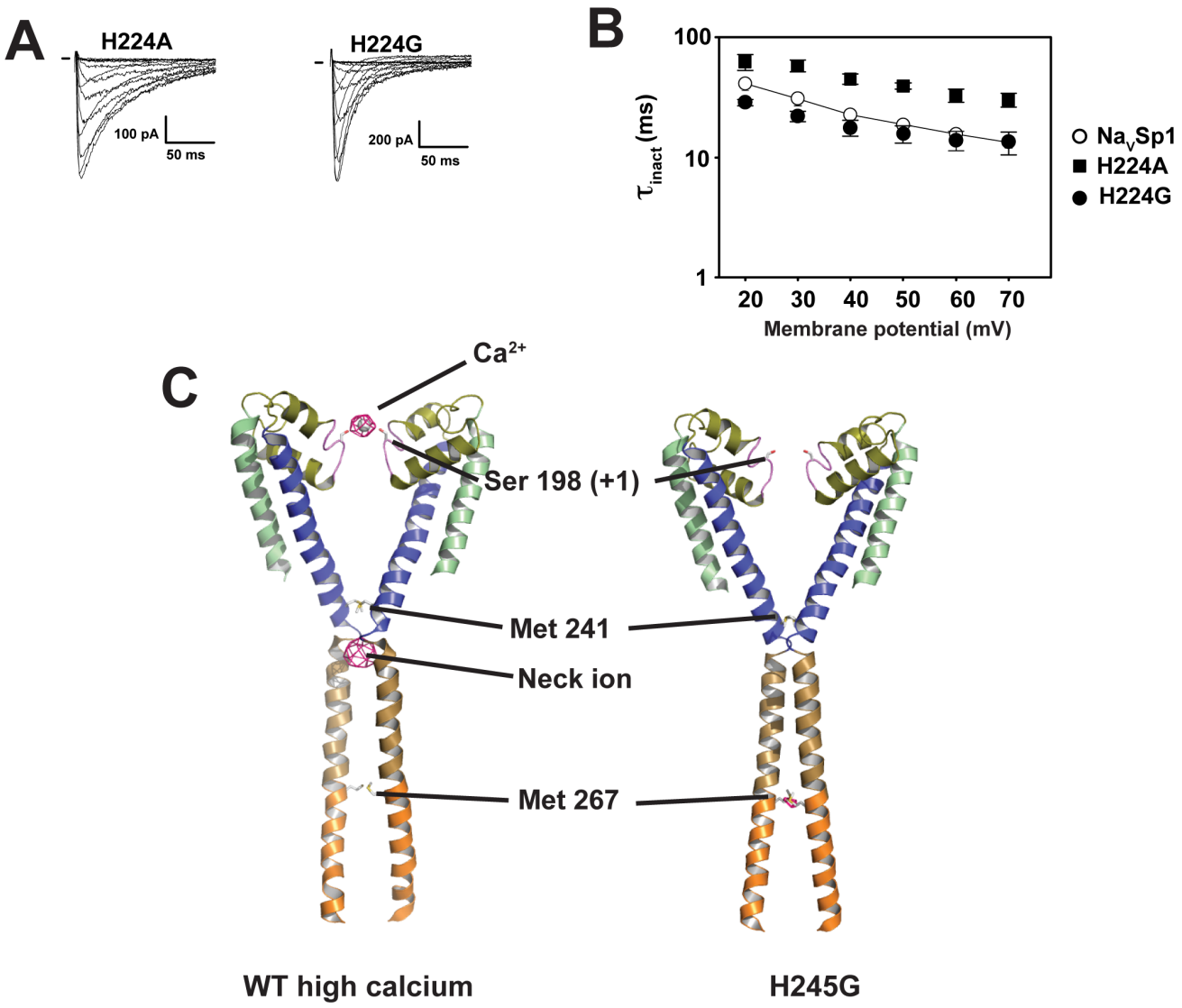


**Supplementary Figure S9 Functional and structural characterization of bend position mutants** **A,** Representative $Na^+$ currents from $Na_VSp1$, H224G, and H224A in response to an activation protocol of -60 to +70 mV in 10 mV steps. **B,** Comparison of inactivation time constants of $Na_VSp1$ and indicated mutants (n = 3-8; error bars are ± s.e.m.) **C,** $Na_VAe1p$ (left) and $Na_VAe1p$ H245G (right) NCS-averaged anomalous difference maps calculated at 6.5 Å contoured at 7σ (high calcium) or at 7.5 Å contoured at 4.5σ (H245G). The H245G structure shows no anomalous peak for either the neck ion or the pore $Ca^{2+}$ ion site.

# Supplementary Figure S10



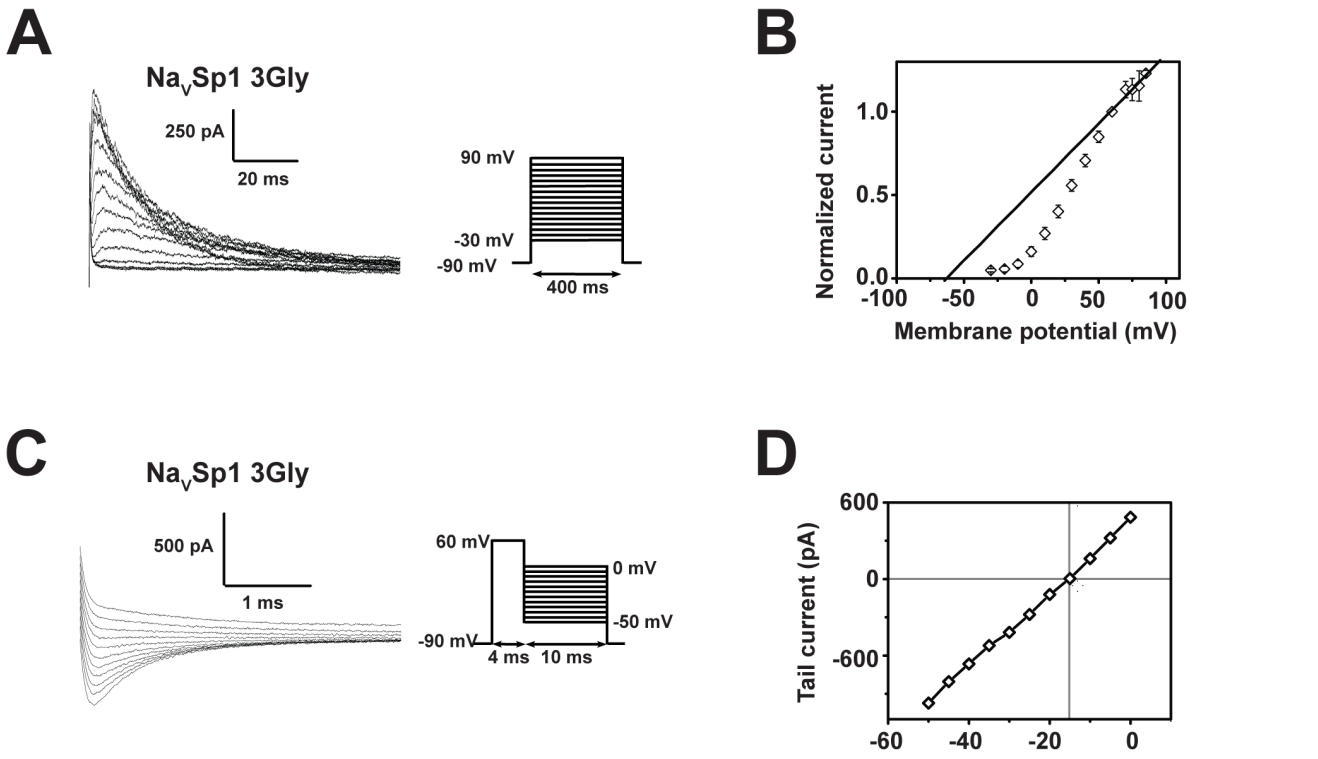


**Supplementary Figure S10 Ion selectivity measurements for $Na_V$Sp1 3Gly A,** Exemplar $Na_V$Sp1 3Gly current trace in presence of 130 mM intracellular $Na^+$ and 107.5 mM extracellular $Ca^{2+}$, in response to an activation protocol, (400 ms depolarizations to -30 to +90 mV in variable steps (10 mV and then 5 mV after 60 mV) from a holding potential of -90 mV, sweep to sweep interval = 5 s). **B,** Normalized current-voltage curve from experiments performed as in '**A**'. Reversal potential can be obtained by linear regression, as indicated. The averaged value obtained by this method (n=5) yields $E_{rev}$ = -77.6 ± 8.1 mV, which gives $P_{Ca}/P_{Na}$ = 0.05 ± 0.02 (n=5) when corrected for the liquid junction potential (-17mV). **C,** Exemplar $Na_V$Sp1 3Gly tail currents in presence of 40 mM intracellular $Na^+$ and 107.5 mM extracellular $Ca^{2+}$, evoked by a step protocol (10 ms from -50 to 0 mV in 10 mV steps, after a 4 ms depolarizing step to 60 mV from a holding potential of -90 mV, sweep to sweep interval = 5 s). **D,** Tail current-voltage curve from '**C**'. Linear regression of data points from different experiments (n =4) shows a reversal potential of -33.0 ± 0.9 mV, when corrected for liquid junction potential (-18mV), which gives a permeability ratio $P_{Ca}/P_{Na}$ of 0.07 ± 0.02. All values are mean ± s.e..

## Supplementary Table S1 Crystallographic data collection and refinement statistics

| | $Na_VAe1p$ – Crystal I High calcium*§ | $Na_VAe1p$ –Crystal I High calcium *† | $Na_VAe1p$ –Crystal II High calcium *§ | $Na_VAe1p$ Low calcium**§ | $Na_VAe1p$ – H245G Low calcium**§ |
|---|---|---|---|---|---|
| **Data Collection** | | | | | |
| Space group | I222 | I222 | I222 | $P4_2$ | I222 |
| Cell dimensions a/b/c (Å) | 147.83 / 161.73 / 162.27 | 147.83 / 161.73 / 162.27 | 147.27 / 161.50 / 161.69 | 181.14 / 181.14 / 94.02 | 157.20 / 161.38 / 165.45 |
| $\alpha/\beta/\gamma$ (°) | 90 / 90 / 90 | 90 / 90 / 90 | 90 / 90 / 90 | 90 / 90 / 90 | 90 / 90 / 90 |
| Collection wavelength (Å) | 1.11587 | 1.11587 | 1.11587 | 1.11587 | 1.70192 |
| Resolution (Å) | 115 – 3.46 (3.65-3.46) | 115-4 (4.22-4.00) | 115-3.8 (4.01 – 3.80) | 120 – 5.50 (5.80 – 5.50) | 75 – 5.80 (6.11 – 5.80) |
| $R_{pim}$ (%) | 4.4 (213.4) | 3.5 (47.0) | 6.7 (138.1) | 3.5 (222.1) | 3.7 (115.3) |
| Mn ($I/\sigma I$) | 8.7 (0.3) | 12.2 (1.9) | 6.0 (0.5) | 9.8 (0.7) | 8.7 (0.7) |
| $CC_{1/2}$ | 0.999 (0.144) | 0.999 (0.784) | 0.999 (0.129) | 0.999 (0.092) | 0.999 (0.136) |
| Completeness (%) | 94.2 (72.3) | 99.9 (100.0) | 99.4 (97.0) | 97.3 (86.1) | 98.7 (98.7) |
| Redundancy | 10.5 (2.8) | 12.6 (11.8) | 8.2 (6.4) | 4.0 (3.7) | 13.1 (13.6) |
| Unique reflections | 24208 | 16743 | 19162 | 9811 | 5978 |
| **Refinement** | | | | | |
| $R_{work}$ / $R_{free}$ (%) | 22.4 / 26.8 | | 22.5 / 27.3 | 26.7 / 29.4 | 26.2 / 31.8 |
| Resolution (Å) | 15.0 – 3.46 | | 15.0 – 3.80 | 15.0 – 5.50 | 15.0 – 5.80 |
| No. of chains in AU | 4 | | 4 | 8 | 4 |
| No. of protein atoms | 4084 | | 4016 | 8086 | 4043 |
| No. of ligand atoms | 11 | | 9 | 0 | 0 |
| RMSD bond lengths (Å) | 0.0110 | | 0.0114 | 0.0103 | 0.0070 |
| RMSD angles (°) | 1.656 | | 1.624 | 1.216 | 0.966 |
| Ramachandran best/disallowed (%) | 92.5 / 0.0 | | 94.6 / 0.0 | 96.2 / 0.0 | 96.3 / 0.0 |

* 200 mM calcium

** 0 mM calcium

§ $Na_VAe1p$ Crystal I using data resolution defined by $CC_{1/2} > 0.1$ (Karplus and Diederichs, 2012).

† $Na_VAe1p$, Crystal I using data resolution defined using a cutoff of Mn ($I/\sigma I$) = 1.9

**Supplementary Table S2 Coiled coil parameters**

| Channel and element (residue numbers) | $Na_VAe1p$ CC (265-285) | $Na_VAe1p$ neck + CC (247-285) | $Na_VAe1p$ neck (247-264) | NaK-$Na_VSulP$ CC (115-139) | NaK-$Na_VSulP$ (104-139) | KcsA (118-160) | KcsA (142-160) |
|---|---|---|---|---|---|---|---|
| Superhelical parameters | | | | | | | |
| Radius (Å) | 7.4 | 7.8 | 8.3 | 7.8 | 8.3 | 7.9 | 8.3 |
| Residues / superhelix turn | 103 | 153 | 317 | 126 | 160 | 816 | 160 |
| Pitch (Å) | 154.1 | 228 | 476 | 7.8 | 8.3 | 1200 | 8.3 |
| $\alpha$-helical parameters | | | | | | | |
| Radius (Å) | 2.24 | 2.27 | 2.30 | 2.32 | 2.32 | 2.33 | 2.37 |
| Residues/turn | 3.57 | 3.59 | 3.61 | 3.68 | 3.67 | 3.69 | 3.76 |
| Rise/residue (Å) | 1.57 | 1.55 | 1.52 | 1.51 | 1.51 | 1.49 | 1.49 |

Comparison of coiled-coil parameters as determined using Twister(Strelkov and Burkhard, 2002)

**Supplementary Table S3 Comparisons of $Na_V$ pore structures**

| | PDB code | Monomer RMSD (Å) | Tetramer RMSD (Å) |
|---|---|---|---|
| **$Na_V$Ab I217C** | 3RVY | 1.1 | 1.2 |
| **$Na_V$Ab WT chains A/B** | 4EKW | 1.2/1.2 | 1.6 |
| **$Na_V$Ab WT chains C/D** | 4EKW | 1.2/1.2 | 1.5 |
| **$Na_V$Rh G208S** | 4DXW | 1.5 | 2.1 |
| **$Na_V$Ms** | 4F4L | 1.0/1.0/1.1/1.1 | 1.3 |
| **$Na_V$SulP cc** | | 1.0 | 1.2 |
| **KcsA four helix bundle** | | 0.6 | 4.6 |

In cases where monomer/monomer superpositions deviated by more than 10%, values are shown for each independent chain.

For the $Na_V$ superpositions residues $Na_V$Ae1p residues 150-239 were compared with the equivalent positions from the indicated Bac$Na_V$ channels.

For $Na_V$SulP cc comparison $Na_V$SulP residues 115-139 are compared with $Na_V$Ae1p 260-284.

For KcsA four helix bundle comparison, KcsA residues 137-151 were compared with compared with $Na_V$Ae1p 266-280.

**Supplementary References**

Karplus, P.A., and Diederichs, K. (2012). Linking crystallographic model and data quality. Science *336*, 1030-1033.

Lomize, M.A., Lomize, A.L., Pogozheva, I.D., and Mosberg, H.I. (2006). OPM: orientations of proteins in membranes database. Bioinformatics *22*, 623-625.

McCusker, E.C., Bagneris, C., Naylor, C.E., Cole, A.R., D'Avanzo, N., Nichols, C.G., and Wallace, B.A. (2012). Structure of a bacterial voltage-gated sodium channel pore reveals mechanisms of opening and closing. Nature communications *3*, 1102.

Payandeh, J., Gamal El-Din, T.M., Scheuer, T., Zheng, N., and Catterall, W.A. (2012). Crystal structure of a voltage-gated sodium channel in two potentially inactivated states. Nature *486*, 135-139.

Payandeh, J., Scheuer, T., Zheng, N., and Catterall, W.A. (2011). The crystal structure of a voltage-gated sodium channel. Nature *475*, 353-358.

Strelkov, S.V., and Burkhard, P. (2002). Analysis of alpha-helical coiled coils with the program TWISTER reveals a structural mechanism for stutter compensation. J Struct Biol *137*, 54-64.

Zhang, X., Ren, W., DeCaen, P., Yan, C., Tao, X., Tang, L., Wang, J., Hasegawa, K., Kumasaka, T., He, J.*, et al.* (2012). Crystal structure of an orthologue of the NaChBac voltage-gated sodium channel. Nature *486*, 130-134.